Aus dem Institut für Diagnostische und Interventionelle Radiologie
der Universität zu Köln
Direktor: Universitätsprofessor Dr. med. D. Maintz

Development and characterization of a bone phantom for MR-HIFU systems
-
Entwicklung und Charakterisierung eines Knochenphantoms für MR-HIFU Geräte

Inaugural-Dissertation zur Erlangung der ärztlichen Doktorwürde
der Medizinischen Fakultät
der Universität zu Köln

vorgelegt von
Janina Strobel
aus Bad Saulgau

promoviert am 07. Juni 2024

Gedruckt mit Genehmigung der Medizinischen Fakultät der Universität zu Köln
Druckjahr 2024

Dekan:	Universitätsprofessor Dr. med. G. R. Fink
1. Gutachter:	Universitätsprofessor Dr. rer. nat. H. Grüll
2. Gutachter:	Privatdozent Dr. med. K. Zarghooni
3. Gutachter:	Privatdozent Dr. med. B. Sabel

Erklärung

Ich erkläre hiermit, dass ich die vorliegende Dissertationsschrift ohne unzulässige Hilfe Dritter und ohne Benutzung anderer als der angegebenen Hilfsmittel angefertigt habe; die aus fremden Quellen direkt oder indirekt übernommenen Gedanken sind als solche kenntlich gemacht.

Bei der Auswahl und Auswertung des Materials sowie bei der Herstellung des Manuskriptes habe ich keine Unterstützungsleistungen erhalten.

Der CT- Datensatz zur Segmentierung der Schweinewirbelsäule und -femurs wurde von Dr. Sin Yuin Yeo erhoben.

Die Auswertung der akustischen Eigenschaften des Polyurethan Materials und des Polyacrlyamid Gels wurde vom Therapy Ultrasound team des Joint Department of Physics/ Division of Radiotherapy and Imaging am Institute of Cancer Research, London, UK erhoben.

Weitere Personen waren an der Erstellung der vorliegenden Arbeit nicht beteiligt. Insbesondere habe ich nicht die Hilfe einer Promotionsberaterin/eines Promotionsberaters in Anspruch genommen. Dritte haben von mir weder unmittelbar noch mittelbar geldwerte Leistungen für Arbeiten erhalten, die im Zusammenhang mit dem Inhalt der vorgelegten Dissertationsschrift stehen.

Die Dissertationsschrift wurde von mir bisher weder im Inland noch im Ausland in gleicher oder ähnlicher Form einer anderen Prüfungsbehörde vorgelegt.

Die in dieser Arbeit angegebenen Experimente sind nach entsprechender Anleitung durch Dr. Lukas Sebeke von mir selbst ausgeführt worden.

Erklärung zur guten wissenschaftlichen Praxis:

Ich erkläre hiermit, dass ich die Ordnung zur Sicherung guter wissenschaftlicher Praxis und zum Umgang mit wissenschaftlichem Fehlverhalten (Amtliche Mitteilung der Universität zu Köln AM 132/2020) der Universität zu Köln gelesen habe und verpflichte mich hiermit, die dort genannten Vorgaben bei allen wissenschaftlichen Tätigkeiten zu beachten und umzusetzen.

Köln, den 06.12.2023

Acknowledgments

I would like to express my sincere gratitude to Holger for the opportunity to undertake this bone phantom project, for guiding me in all steps of the journey but also for giving me experimental freedom and trust to follow my own ideas. You truly know how to spread the enthusiasm for HIFU! Of course, I also need to thank you for your patience while waiting for the most recent drafts of this thesis!

I could not have undertaken this project without my supervisor Lukas, thank you for supporting me from my first steps at the HIFU console right to the final version of this thesis. I am extremely grateful that you shared your immense knowledge regarding HIFU, phantoms, 3D printers and also python programming with me. I am genuinely lucky to have found such a dedicated supervisor and I will keep our shared experiments, lunch- and coffee breaks in the best memory.

I will definitely not forget the time spent with the ‘rat pack’ (Patrick, Juan and Claudia): With you even the longest HIFU experiment was always fun!

All in all, I am extremely grateful for my time in the AG Grüll and especially for meeting such kind, helping and inspiring researchers.

Last but not least I want to thank my partner Gabriel for coping with me and my mood during the writing process of this thesis.

Table of contents

List of abbreviations

APS..... Ammonium persulfate
B_0 .....External magnetic field
B_{loc} .....Local magnetic field
c ..... Speed of sound
CE.....Conformité européenne
CEM43..... Cumulative equivalent minutes
CT .....Computed tomography
c_v .....Heat capacity
DISC ..... Direct skin cooling
FA .....Flip angle
FAIS.....Finite- amplitude insertion- substitution method
GRE ..... Gradient recalled echo
HIFU ..... High-intensity focused ultrasound
I_{TA}.....time averaged acoustic Intensity
MR .....Magnetic resonance
MR-HIFU.....Magnetic resonance-guided high-intensity focused ultrasound
p_0 ..... Pressure amplitude
PC..... Polycarbonate
PLA..... Polylactide
PMMA .....Polymethyl methacrylate
PVA.....Polyvinyl alcohol
$\dot{Q}$ .....Heating rate per unit volume
R^2 ..... Correlation coefficient
RFA..... Radiofrequency ablation
SE .....Standard error
STL.....Standard tessellating language
t .....Treatment time
T .....Temperature
TE..... Echo time
TEMEDN,N,N',N'-Tetramethyl ethylenediamine
T_{max}..... Maximum temperature
T_{mean} .....Mean temperature
TR ..... Time of repetition
γ .....Gyromagnetic ratio
ρ ..... Density
σ ..... Screening constant
ω .....Larmor frequency
α ...Ultrasonic amplitude absorption coefficient

1. Zusammenfassung/Summary

In der vorliegenden Studie wurde ein Knochenphantom zur Qualitätskontrolle von MR-gesteuerten hoch-intensivem fokussierten Ultraschall (MR-HIFU) Behandlungen entwickelt und charakterisiert.

Hoch intensiver fokussierter Ultraschall (HIFU) ist ein vielversprechender Behandlungsansatz, der auf einer komplett nicht-invasiven Erhitzung von Gewebe basiert. Die Steuerung und Temperaturkontrolle des Ultraschalls erfolgen mittels MR-Bildgebung. Die derzeitige Hauptanwendungsgebiete von MR-HIFU sind die Behandlung von Uterusmyomen, Desmoid Tumoren, Knochenmetastasen und der Adenomyose.

Derzeit existieren mehrere verschiedene MR-HIFU Systeme, die durch die Firmen Profound Inc, (Mississauga, Canada) und Insightec Corp. (Haifa, Israel) vertrieben werden und sich jeweils durch die verwendeten Schallköpfe, Ansteuerungssoftware und MR-Systeme unterscheiden. Dies kann zu Herausforderungen beispielsweise bei Multicenter Studien führen, da die Vergleichbarkeit der einzelnen Geräte schwer vorherzusagen ist. Aus diesem Grund wurde in dieser Studie ein Knochenphantom zur Qualitätskontrolle von MR-HIFU Geräten und Behandlungsweisen entwickelt.

Das entwickelte Knochenphantom sollte aus einem widerstandsfähigen Material sein, das auch wiederholten Behandlungen mit fokussiertem Ultraschall standhält. In dieser Arbeit wurden mehrere Materialien getestet, wobei das Polymer Polyurethan, aus dem auch Ultraschall-Absorber hergestellt werden, sich als am geeignetsten erwies. Dieses Material wurde dann in einem Gel bestehend aus Polyacrylamid eingebettet und verschiedenen Ultraschallbehandlungen ausgesetzt, wobei mittels MR Thermometrie die Erwärmung an der Knochenphantomoberfläche gemessen wurde. Die Reproduzierbarkeit der Temperaturentwicklung bei HIFU-Experimenten wurde mittels wiederholter standardisierter Bestrahlungen und Messungen über einen Zeitraum von mehreren Wochen geprüft. Dabei zeigte sich eine reproduzierbare, kontinuierliche Hitzeentwicklung.

Zusätzlich wurden die Erwärmung des Phantoms unter dem Einfluss verschiedener Ultraschallleistungen sowie zwei unterschiedliche Ansätze der Bestrahlungsplanung untersucht. Die beiden Ansätze der Bestrahlungsplanung unterscheiden sich in der Positionierung des Brennpunktes bzw. durch die Vewendung unterschiedlicher Schalleistungen. Es zeigte sich ein linearer Zusammenhang zwischen angewandter Energie und Hitzeentwicklung. Die beiden Ansätze zur Bestrahlungsplanung zeigten keinen signifikanten Unterschied hinsichtlich des abladierten Volumens im angrenzenden Polyacrylamid Gels.

Das entwickelte Knochenphantom kann in Zukunft dazu genutzt werden, MR-HIFU Geräte vor Behandlungen von Erkrankungen des Knochens zu kalibrieren und ist daher ein wichtiges Werkzeug in der möglichen Durchführung von Multicenter-Studien. Die Ergebnisse des

Vergleichs der Behandlungsplanungsansätze und des Einflusses der Energiestärke haben aufgrund der geringen Anzahl an Wiederholungen der Experimente nur eine bedingte Aussagekraft, können jedoch als Indikator für zukünftige Forschung gewertet werden.
Ein weiterer Schwerpunkt dieses Projekts war die Herstellung von realistischen Formen des Knochenphantoms. Es wurden zwei verschiedene Möglichkeiten zur Herstellung eines maßstabsgetreuen Wirbelsäulenphantoms entwickelt.

In this study, a bone phantom was developed and characterised for quality control of MR-guided high-intensity focused ultrasound (MR-HIFU) treatments.
High-intensity focused ultrasound (HIFU) is a promising treatment approach based on the completely non-invasive heating of tissue. MR imaging is used to guide and measure the temperature of the ultrasound. The main applications of MR-HIFU are currently the treatment of uterine fibroids, adenomyosis, desmoid tumours and bone metastases.
The main advantage of MR-HIFU is the completely non-invasive approach. This makes it a very patient-friendly and low-risk procedure. MR-HIFU treatment has already been approved for many applications, but randomised controlled trials are currently lacking to make this type of treatment even more widespread.
Currently, there are several different MR-HIFU systems on the market which are mainly manufactured by the companies Profound Inc. (Mississauga, Canada) and Insightec Corp. (Haifa, Israel). They differ regarding the transducers, software and MR-systems in use. This can lead to challenges, for example in multicentre studies, as the comparability of the individual devices is difficult to predict. For this reason, a bone phantom was developed in this study for the quality control of MR-HIFU devices and treatment methods.
The developed bone phantom should be made of a durable material that can withstand repeated treatments with focused ultrasound. In this thesis, a variety of materials was tested, whereas the polymer polyurethane, which is also used to manufacture ultrasound absorbers, was found to be the best candidate. This material was then embedded in a phantom gel consisting of polyacrylamide and exposed to different ultrasound treatments. The heating on the surface of the bone phantom during the ultrasound exposure was measured via MR-thermometry. The reproducibility of the temperature development of the HIFU experiments was tested by means of repeated standardised sonications and measurements over a period of several weeks. This showed a reproducible, continuous heat development.
In addition, the influence of different power levels on the heating at the phantom surface and two different approaches to sonication planning were investigated. The two approaches to sonication planning differ regarding the positioning of the focal point and regarding the applied power level and sonication time. A linear relationship between applied energy and heat

development was found. The two approaches to sonication planning showed no significant difference regarding the heated volume of the surrounding polyacrylamide gel.
The developed bone phantom can be used in the future to calibrate MR-HIFU devices prior to treatments of bone diseases and is therefore an important tool in the implementation of future multicentre studies. The results of the comparison of the treatment planning approaches and the influence of the energy level have only limited significance due to the low sample size of the experiments but can be taken as an indicator for future research.
An added focus of this project was the manufacturing of a more realistic shape of the bone phantom. Two different ways of manufacturing a to scale spine phantom were developed.

2. Introduction

2.1 Thermal therapy

Cancer therapy is dominated by surgical methods, radiotherapy, chemotherapy and immune therapy. Despite decades of research in the field of cancer, some types of cancer are still hard to treat. Besides the established types of cancer treatment, much research is conducted in alternative treatment methods. One of them is the thermal therapy.

Using heat for treating non-malignant growth has been a method since first described in the ancient Egyptian times.[1] In the past, therapeutic heat was commonly applied using conductive heating, i.e. cauterization by using a hot solid or treatment of fever/ infections by hyperthermic applications (hot baths or hot stones). In 1868 the surgeon Busch observed that a fever caused by an erysipelas reduced the growth of a sarcoma.[2] This finding triggered Coley to induce fewer in cancer patients using a bacterial derived toxin giving birth to the field of hyperthermia.[3] Subsequently, many devices were invented and explored to induce hyperthermia in deep-seated tissue.

The main idea of these methods is still used today in the form of hyperthermic perfusion.[4-7] Other techniques induce heating using e.g. electromagnetic radiation or ultrasound waves in tissue, which allows the non-invasive heating of deep-seated tissues.[8,9] At present, thermal therapy is a considerable treatment option not only for cancer, but also for non-malignant conditions.

Thermal therapy can be divided into the following categories:

Hyperthermia: Using temperature levels between 41 and 45 °C to achieve mild cytotoxic effects and mainly used as an enhancer of chemotherapy and radiofrequency therapy [10-13] and for stimulation of immunological effects. [14,15]

Thermal ablation: Temperatures above approx. 56 °C induce rapid cell death via the denaturation of proteins and the destruction of cell membranes and are used in therapy of various cancer types. [16,17]

The biological effect of the heating depends on the applied temperature, the duration of the heating and the type of tissue. During initial experiments with cell lines it was found that the relation between cell death, temperature and heating duration follows an Arrhenius curve.[18,19] Following this realization, the thermal dose concept was introduced to facilitate standardization:[20] Treatments with different temperatures (T*)* and treatment times (*t*) can be compared by converting the applied temperature and time to a corresponding treatment time at 43 °C known as cumulative equivalent minutes (CEM43):

$$CEM43 = \int_{t0}^{t} R^{\frac{43\,°C - T(t')}{1\,°C}} dt \tag{1}$$

$$R = \begin{cases} 0.5, T > 43\,°C \\ 0.25, T \leq 43\,°C \end{cases}$$

The different values for the parameter R under and above 43 °C root from a breakpoint in thermotolerance in cells.[21,22] The values of R and the breakpoint temperature, however, are a convention and may vary depending on the type of cells and tissue treated.[23] Therefore, the exact thermal dose value at which proteins denature and cells, respectively tissues break down is different for each cell line or tissue.[24,25] For example, Chinese hamster ovary cells have a lower thermotolerance than human melanoma cells.[24] With respect to these differences in thermal sensitivity a threshold of 240 mins regarding the CEM43 value was chosen to predict a successful thermal ablation, since most tissues regardless of origin or malignancy show coagulative necrosis at this value.[23,26]

2.2 MR-HIFU

The demand for non- or minimally invasive treatment options has been rising over the last decades.[27] With MR-HIFU, it is possible to treat the patient with no incision at all. The benefits for the patients and economy are obvious:[28,29] Shorter hospital stays up to outpatient procedures and less post-interventional complications such as bleeding or infection. The following section is focused on the technical background of this novel treatment approach.

2.2.1. Focused ultrasound

The first investigation of the interaction between biological tissue and high-intensified focused ultrasound was done by Lynn et al. in 1942.[30] Those first insights were followed by years of technical evolution, but the basic principle, which is similar to focusing sunlight through a convex lens, still remained the same.

The ultrasound waves are generated by a transducer with piezoelectric elements. The piezoelectric material inside is stimulated by an alternating voltage and contracts and expands in relation to the applied voltage. Because of the mechanical disturbance, ultrasound waves are produced. A HIFU-transducer is usually operating at frequencies around 1 MHz[31], which is lower than standard diagnostic ultrasound (2-15 MHz).[32] The optimal frequency for the various MR-HIFU treatments depends on the type of treated tissue. An increasing frequency leads to a higher heat deposition but also to an decrease in penetration depth.[31]

As the name implies, HIFU works with a higher intensity than diagnostic ultrasound: Typical intensity (spatial and temporal average) values at the focal spot are around 1000 W/cm^2. [33]

Another difference to diagnostic ultrasound is the direction of the emitted ultrasound waves: While diagnostic ultrasound is using a linear or divergent direction of flow, the HIFU transducer focuses the waves on a point and thereby concentrates the energy of the beam.

Ultrasound beams can be focused by a spherically shaped transducer, acoustic lenses, reflectors or phased array transducers.[34] Most common in clinical use are phased array transducers, since they offer the best control over the deposited acoustic energy.[34] A phased array transducer consists of a large number of piezo-electric elements, which each emit a roughly spherical wave. By driving the individual elements in a coordinated manner, an acoustic focus with large pressure amplitudes can be generated. The long axis of the focal volume varies from 5-30 mm depending on frequency and aperture of the transducer, with diameters between 1-5 mm.[34] Furthermore, modulation of the phase allows for electronic beam steering, where the focus point can be rapidly moved through the target tissue.

While propagating through the human body, ultrasound waves interact with tissue in various ways. They can be attenuated by absorption, reflection, refraction or scattering.[35] Absorption is caused by energy dissipation leading to vibration and rotation of molecules in the tissue resulting in heating via friction.[36] This effect leads to rapid tissue heating within the focal

volume. Surrounding tissue heats up more slowly due to the lower acoustic intensities. Refraction and reflection occur when an ultrasound wave passes the interface between two media. The direction of the reflected/ refracted wave follows Snell's law. This physical phenomenon is used, for instance, in diagnostic ultrasound, where the amplitude of the reflected wave is converted into a bright-scale and eventually an image.

The attenuation of ultrasound waves can lead to challenges during a HIFU treatment: In order to achieve a sufficient absorption of ultrasound energy in the desired treatment region, the beam path must be free of acoustic barriers like gas-filled bowel (relevant e.g. in treatment of the pancreas[37]) or bone.[38] Furthermore, heating between the transducer and the targeted tumour must be managed to prevent injury of healthy tissue.

The heating rate per unit volume $\dot{Q}$ at which heat is produced is proportional to the ultrasonic amplitude absorption coefficient α (which increases with frequency) and the time averaged intensity of the ultrasonic wave I_{TA}.

$$\dot{Q} = 2\alpha I_{TA} = \frac{\alpha pp*}{\rho \cdot c} = \alpha \frac{p_0^2}{\rho \cdot c} \tag{6}$$

with ρ as density, p_0 as the pressure amplitude and c as the sound speed. Consequently, the rate of temperature rise $\Delta T/\Delta t$ at the bone interface increases linearly with the applied acoustic intensity.[39]

$$\Delta T = \frac{1}{C_v} \cdot \dot{Q} \cdot \Delta t = \frac{\Delta t}{C_v} \cdot \alpha \frac{pp*}{\rho \cdot c} = \frac{1}{C_v} \cdot \alpha \cdot \frac{p_0^2}{\rho \cdot c} \cdot \Delta t \tag{7}$$

with C_v as the heat capacity.

The equation above does not take into account the in vivo perfusion of the tissue adjacent to the bone surface, which adds to heat dissipation. A mathematical model which considers this relationship between heat transfer and blood flow is the Pennes' bioheat equation.[16,40,41]

2.2.2. Thermometry

Guidance of the focused ultrasound can be achieved either through diagnostic ultrasound or magnetic resonance imaging. MR images offer a higher soft tissue contrast and a better resolution than ultrasound images.[17,42] On the other hand, diagnostic ultrasound guidance provides images in real time, but cannot provide detailed information about the achieved temperature.[43] MR-guidance instead provides near real-time temperature information.[44]

MR-thermometry is based on the principle of proton resonance frequency shift (PRFS) and was first introduced by Ishiara et al. and De Poorter et al. in 1995.[45,46] The exploited physical phenomenon is, to a good approximation, the linear decrease of the water proton resonance frequency with increasing temperature described by the temperature-dependent water

chemical shift α = -0.01 ppm/°C. The shift is caused by a weakening of the screening effect of the hydrogen bonds in water molecules. Consequently, the local magnetic field B_{loc} changes:

$$B_{loc} = B_0 \times (1 - \sigma) \quad (1)$$

With B_0 as the external magnetic field and σ as the screening constant, which depends linearly on the local temperature:

$$\sigma(T) = \alpha T \quad (2)$$

where α is the proportionality constant (α =−1.03 ± 0.02 · 10^{-8} 1/°C for -15 °C<T< 100 °C). This leads to a linear correlation of the protons Larmor frequency ω with temperature:

$$\omega(T) = \gamma B_0 (1 - \sigma) \quad (3)$$

with γ as the gyromagnetic ratio, defined as the ratio of the magnetic momentum and the angular momentum of the proton. To calculate the local temperature, the difference of the current Larmor frequency φ(T) after a certain time t to the baseline Larmor frequency of unheated tissue ($\varphi(T_{ref})$) is measured via the phase shift in a gradient recalled echo (GRE) image.

$$\Delta T = \frac{\varphi(T) - \varphi_{(Tref)}}{\gamma \alpha B_0 t} \quad (4)$$

As this technique is only suitable for the measurement of temperature differences, the resulting ΔT is added to the baseline temperature of the unheated tissue, which must be determined by other means.[44,47]

The PRFS method provides temperature measurements with an accuracy of ΔT < 1 °C in stationary tissue and ΔT < 2-3 °C in moving tissue.[48] MR-HIFU systems in clinical usage work with 1.5 or 3.0 Tesla MR scanners.[49]

2.3 Clinical applications of MR-HIFU in bone related conditions

Applications of MR-HIFU have become increasingly widespread over the last few decades. While the first U.S. Food and Drug administration (FDA) approved focused ultrasound device was only in use to treat glaucoma,[50] in 2022 treatment of 32 clinical conditions gained regulatory approval in the world, eight of them are approved by the FDA and in 96 clinical indications there is ongoing research.[51] Currently, the most widespread applications of MR-HIFU are the ablation of uterine fibroids and bone metastases. The Sonalleve® System (Profound Medical Inc. Canada) is CE-approved for both indications.

MR-HIFU treatment of bone differs from other conditions because of the particular acoustic and thermal properties of the bone cortex.[52,53] It has a higher absorption rate and a lower conductivity of acoustic energy than soft tissue and has almost no perfusion. Moreover, the surface between bone cortex and surrounding tissue causes reflection of ultrasound waves as well as shear waves inside the bone cortex.[54] These circumstances together lead to a fast heating of the bone cortex and the consecutive ablation of the tissue surrounding it.[35]

The following sections are focused on MR-HIFU treatment of bone related indications.

2.3.1. Bone metastases

Bone is a common site for metastases of primary solid tumours (e.g. breast or prostate cancer). Bone metastases can occur in any bone structure in the body, the most typical locations are the axial skeleton, ribs and pelvis.[55]

Breast and prostate cancer are the types of cancer with the highest overall incidence rate. Roughly one in eight women (lifetime risk 12.8%) develops breast cancer and one in nine men (lifetime risk 11.6%) develops prostate cancer.[56] Here, the prevalence of bone metastases is 4% in patients with breast cancer and 6% in patients with prostate cancer.[57] Also other types of cancer, such as lung cancer, thyroid carcinoma or renal cell carcinoma, metastasize into bone.[58] As a result, it is a condition which affects many patients and therefore needs continuous research.

Bone metastases clinically present with pain, hypercalcemia and a higher risk of fracture which can also lead to spinal instability.[59] Bone metastases severely reduce quality of life in end stage cancer diseases[60,61] and current treatment aims only for palliative pain relief and prevention of further spread. Pain arises as a consequence of inflammation due to the damaged bone and also compression of surrounding nerves.[62] Typical treatment consists of local radiation, bisphosphonates, denosumab, analgesia and surgical stabilisation if necessary.[63,64]

Despite those numerous approaches to treat bone metastases, there are still patients who suffer from pain even if current treatment options are optimized.[65,66] As an example, not all patients respond sufficiently to radiation therapy, some patients even do not report any pain relief at all.[67,68] The effect of radiation therapy is also not immediate, it can take up to weeks to

reach the full effect of the therapy. Furthermore, even after an initially successful radiation treatment, the pain can recur.[65,69]

Due to these challenges in pain therapy, a lot of research is being conducted in this field and one alternative treatment is MR-HIFU.[70]

The focused ultrasound beam ablates the highly innervated periosteum and therefore interrupts pain signalling.[71] In addition, the tumour shrinks after the treatment.[71,72] MR-HIFU treatment has been shown to be effective, meaning an overall response to pain palliation in 79% of patients with 50.5% of the responders presenting a complete response (pain score 0 after treatment) in a systematic review.[73,74] A big advantage compared to radiation treatment is the repeatability of MR-HIFU treatment, since it is free of ionizing radiation. Furthermore, pain relief sets in within the first days after MR-HIFU treatment compared to weeks after radiation treatment.[73,75-78]

Currently, MR-HIFU is not used as a first line treatment but only as a salvage treatment in case of non-responders or recurrence after radiation. Clinical trials specifically comparing MR-HIFU to radiation therapy are already ongoing to investigate if it should be considered a first line treatment.[70]

2.3.2. Facet joint pain

Lower back pain is an extremely common and growing health problem affecting almost a third, (31,0%)[79] of the global population. It is a leading cause for disability at ages up to 45 years, thus leading to immense social and also economic pressure.[80] Lower back pain can originate from various causes: Amongst them, facet joint osteoarthritis is considered to cause 15-45% of the cases.[81,82]

Current German guidelines suggest a conservative treatment consisting of non-steroidal anti-inflammatory drugs (NSAIDs), muscle relaxant agents, infiltration with a local anaesthetic in combination (optional) with cortisone, ergotherapy, physiotherapy and manual therapy.[83]

If conservative treatment and injections show insufficient results, ablation of the medial branch nerve by radiofrequency, cryoablation or MR-HIFU serves as an alternative.[83-85]

Patients should be carefully selected for this treatment, since back pain can root from several different causes. Depending on the origin, not every back pain patient responds to ablation methods.[86]

The ablation techniques have in common that the signal transmission of pain is interrupted by heating and therefore destroying the medial branch nerve. In comparison to the conservative treatment approach, ablation is more sustainable regarding pain control and functional improvement.[87]

The advantage of MR-HIFU as a treatment tool is the radiation-free and non-invasive approach, which reduces the risk of infection and bleeding rate to an absolute minimum.[88]

Furthermore, guidance via MRI offers a high quality image of the surrounding tissue and potential organs at risk combined with a real-time feedback of temperature rise, which is unique among the currently existing guidance methods.[85]

Prior research in terms of preclinical swine experiments[88,89], single case reports with patients [90,91] and a pilot study with 18 patients[92] showed the safety, feasibility and efficacy of MR-HIFU.

2.3.3. Osteoid osteomas

Osteoid osteoma is a benign but painful skeletal tumour that affects mostly young patients up to the age of 30. It is the third most common benign bone tumour.[93] Typical lesion sites are the long bones, especially diaphysis of femur and tibia, but also the spine and any other places in the skeleton.

Symptoms present with nocturnal pain which responds well to NSAIDs. In case of spine infiltration painful scoliosis can occur.[93] Definite treatment usually consists of surgical extraction or, nowadays more common, percutaneous CT-guided radiofrequency ablation (RFA).[94] MR-HIFU is a very interesting treatment alternative in this case, because it is completely free of ionizing radiation, which is an important benefit for younger patients. Furthermore, it does not require the use of needle-like RFA probes.

While focused ultrasound for bone metastases and facet joints mainly aims on pain reduction by impairing the highly innervated periosteum, the goal of focused ultrasound in this application is the destruction of the bone tumour itself. This seemed unfeasible at first sight, because cortical bone absorbs and reflects most of the acoustic energy. However, osteoid osteomas are smaller and usually do not reach as deep into the bone as for example bone metastases. Studies showed that because of the particular lesion size and composition of osteoid osteomas, treatment with focused ultrasound ablates also the bone itself and not only the surrounding tissue.[95,96] At the same time, the presence of thick cortical bone over the nidus of the osteoid osteoma can reduce the effectiveness of a MR-HIFU treatment as penetration of HIFU into the bone is limited.[97]

According to the outcome of clinical feasibility and safety studies, MR-HIFU treatment is feasible, safe, and effective: Treatment success was comparable to radiofrequency ablation with a reported success rate of 83-100%. The treatment with MR-HIFU is also considered a very safe treatment option, since the rate of adverse events was shown to be extremely low.[98-102]

The minimization of adverse events and the completely non-invasive approach may result in lower overall costs, but neither specific cost analyses nor randomized trials have been described in the literature yet.[102]

2.4 Current challenges in MR-HIFU treatment of bone diseases

2.4.1. Technical challenges

Treatment with MR-HIFU has its limitations: For example, not every patient is suitable for a treatment. If the desired treatment region is too deep inside the body, especially relevant in obese patients, it cannot be reached by a standard transducer with a focal length of 14 cm in a Sonalleve® System.[103] Also, one must consider the possible ultrasound-tissue interaction in the beam path: Some tissues like bone or intestine filled with gas reflect ultrasound waves and interfere with the focusing.[104,105]

Thermometry in tissues with a certain chemical composition can be challenging. Adipose tissue like breast tissue or also bone marrow is not sensitive due to the low water content and the absence of hydrogen bonds.[106] Therefore, treatments in regions with a high proportion of fat tissue are only possible to a limited extent.[36] Cortical bone has an even lower water content and a shorter T_2 relaxation time, which makes it basically impossible to receive temperature information by the PRFS method in bone.[107,108] In clinical practice, the temperature information of the adjacent soft tissue is used to obtain a temperature feedback and determine if the sonication was successful.

2.4.2. Calibration of the transducer

The idea of rapidly heating and therefore destroying tissues has enabled a whole new branch of cancer treatment. But this powerful method needs to be controlled to ensure that the tissue is heated in exactly the right place. To ensure the patient's security and consistent treatment outcomes, reliable measurement and characterization tools are needed.

To date, there is no universally accepted method to calibrate focused ultrasound transducers. According to a survey of Shaw et al. in 2016, the most common calibration method is the use of hydrophones, followed by measurement of the acoustic output or input power and also the use of phantoms.[109] Interestingly, a small fraction of MR-HIFU users did not use any routine calibration method at all and less than 50% stated that they could characterize their HIFU-equipment satisfactorily. Medical ultrasound in general is usually characterized by hydrophones.[110] But the characterization of the acoustic field of a HIFU-transducer by hydrophones remains challenging: A standard hydrophone simply breaks when exposed to focused ultrasound treatment intensities.[111] A way to avoid this is the extrapolation of measurements made at lower intensities.[112] However, this method of calibration is too time-consuming for daily practise.

For routine quality assurance e.g. before a treatment, the use of a phantom is recommended.[113] Over the past years, several unique models of phantoms have been proposed: Most of them are based on acrylamide[114] and mimic the acoustic properties of tissue

by addition of bovine serum albumin.[115] Some phantoms also change their colour when they are prepared with a thermochromic ink.[116,117] But so far, no phantom with the intention to mimic bone has been extensively described and published.

2.4.3. Reporting and comparison of treatments

The outcome of a MR-HIFU therapy depends not only on the experience of the performing clinician,[118] but also on the MR-HIFU system in use and the integrated treatment protocol. Over the past decades, MR-HIFU grew into a research area of great interest. Numerous new applications, technical improvements and clinical trials were published. However, there was limited attention to setting standards for the exact description of the treatments and standardisation. Therefore, comparison of MR-HIFU treatments between different clinical sites is currently challenging.

But not only do the MR-systems vary, the treatment protocols can also differ. Bone metastases can be treated in a direct volumetric heating approach, where the focal point is located directly on the bone surface and moves in concentric circles in order to ablate a bigger surface area.[103] Electronic beam steering allows to for sonication cell sizes from 4 mm to 16 mm. Alternatively, the indirect approach can be used in which the focal spot is placed at a certain distance behind the bone surface where the intersection of equivalent diameter between surface and ultrasound cone is heated (Figure 1).[119]

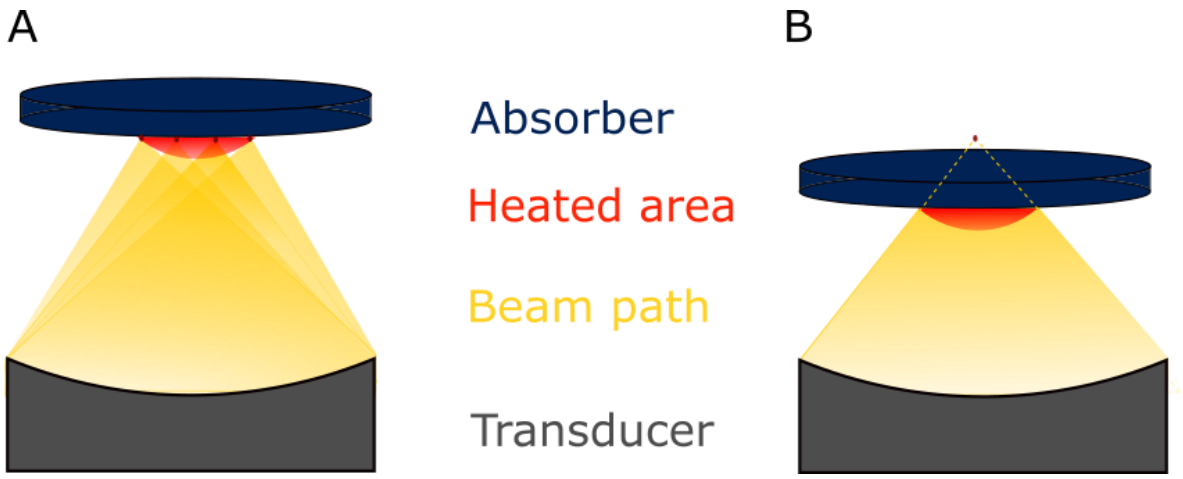

Figure 1: Two different MR-HIFU treatment protocols with A: direct approach using beam steering and B: indirect approach with the focal spot behind the surface.

Finally, due to the differences which parameters of the treatment are adjustable depending on the manufacturers, there is yet no standard on how to describe the treatment sessions in a complete and unambiguous way in publications. Treatment protocols employed on different devices therefore cannot be properly compared.[120]

2.5 Aim of this thesis

Since there is more than just one MR-HIFU device on the market, the question arises if the different devices and available treatment protocols can be compared. Especially in multicentre trials it is important to establish treatment protocols which are standardized.

The first objective of this thesis is to develop a bone phantom, which allows to characterize different MR-HIFU devices and bone treatment schemes in a systematic and reproducible manner. Important aspects that need to be addressed are:

- Reliability and reproducibility:
  The phantom should lead to a reproducible temperature increase for the same sonication.
- Reusability and shelf life:
  The phantom should not degrade over time to allow testing and quality control of (different) MR-HIFU systems at any desired time point.
- Handling and Workflow:
  The end-users of MR-HIFU systems (physicians), who are not necessarily experts in ultrasound measurements, should be able to perform the calibration easily and within the current workflow.

As a next step, this phantom can be used to compare different sonication settings and treatment protocols.

The second objective of this thesis is the production and testing of a more realistic bone phantom with a shape reproducing the original bone (femur, spine etc.). This phantom can be used in treatment simulations to investigate safety and feasibility issues or as a training phantom for physicians.

3. Materials and methods

3.1 Manufacturing

The bone phantom consists of two parts: An object representing the bone, a polyurethane absorber to prevent reflections at the back of the phantom and a polyacrylamide gel representing the soft tissue.

The object representing the bone was embedded in polyacrylamide which was poured in a cylindrical plastic container (Figure 2). The polyacrylamide was created using a composition resembling the formulation by Negussie et al. (Table 1).[117] All used chemicals were purchased from Sigma Aldrich (Sigma-Aldrich Corporation, St. Louis, Missouri, USA).

Figure 2: Polyurethane disk in a plastic container embedded in polyacrylamide.

Table 1: Components of the polyacrylamide gel; (v/v): Volume fraction, (w/v): Weight fraction.

Component	Quantity
Degassed water	82.24% (v/v)
Bis-acrylamide	27.55% (v/v)
N,N,N',N'-Tetramethyl ethylenediamine (TEMED)	0.21% (v/v)
Ammonium persulfate (APS)	0.21% (w/v)

First, the acrylamide and TEMED were mixed with degassed water under magnetic stirring for approx. 20 s. To initiate polymerization APS was added under continued stirring for 10 s. Immediately after those 10 s the still liquid gel was poured into the plastic container up to the desired height of the polyurethane disk. After letting the polyacrylamide gel harden for 10 min, the polyurethane disk was placed on top of the gel layer in the middle of the aperture of the plastic container. In the meantime, another gel was prepared using the same method as described above and poured onto the existing gel with the polyurethane disk to fill the container up to the top. After another 10 min of hardening, the container was sealed with the corresponding cover and a layer of plastic wrap in between to avoid shrinking of the gel. The plastic wrap was removed immediately before sonication.

3.2 Bone phantom materials

Various materials (polyurethane, Verowhite® (a synthetic resin), polycarbonate (PC) and polymethyl methacrylate (PMMA)) were embedded in a polyacrylamide gel and treated with power ranges from 10-80 W or 120- 190 W for 16 s. After that, the polyacrylamide gel was removed and the used materials checked for visible damage.

Acoustic parameters of the polyurethane disk and polyacrylamide gel were measured using the finite-amplitude insertion-substitution method (FAIS) and can be found in the appendix. The measurements were performed by the Therapy Ultrasound team of the Joint Department of Physics/Division of Radiotherapy and Imaging at the Institute of Cancer Research, London, UK.

3.3 Bone phantom shape: Porcine spine and femur model

3.3.1. Standard way of manufacturing

For the segmentation a pre-existing dataset of high-resolution CT scans of the abdomen of a landrace pig was used. The segmentation was performed with the software 3D-Slicer.[121] To differentiate between bone and tissue an automatic threshold approach (Otsu) was used, followed by an island command to isolate the connected bone structure and remove the tissue from the segmentation. Median smoothing was added with a kernel size of 2 mm.

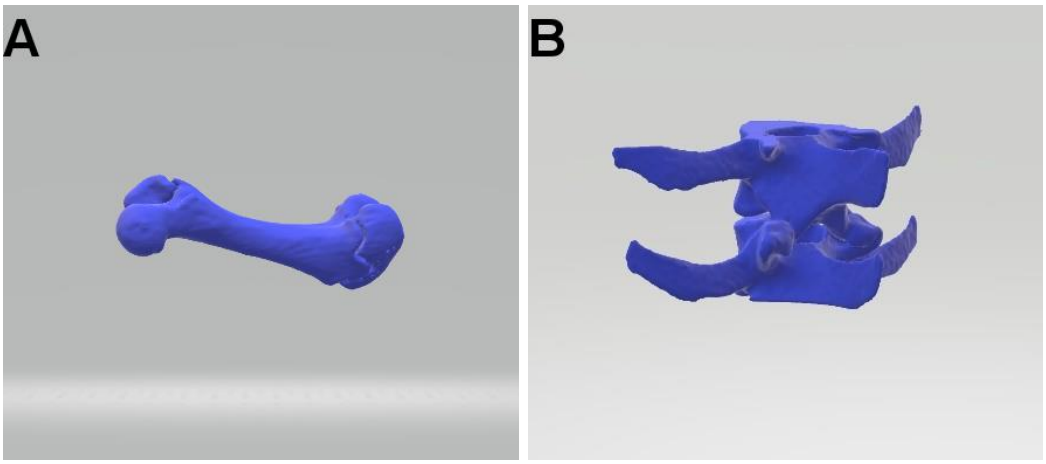

Figure 3: Segmentation of porcine femur (A) and spine (B).

The resulting 3D model (Figure 3) was exported in a STL (standard tessellating language) file and imported in the MeshMixer software (Autodesk; San Rafael, California, version 3.5.474) which was used for creating a mould (Figure 4). An extrusion of 3 mm was applied and the original model was subtracted from the result. A plane cut was made at the height of the processus spinosus in the spine model. A sagittal cut was made through the femur. This resulted in two half-forms of spine and femur. Finally, the resulting meshes were exported as STL files.

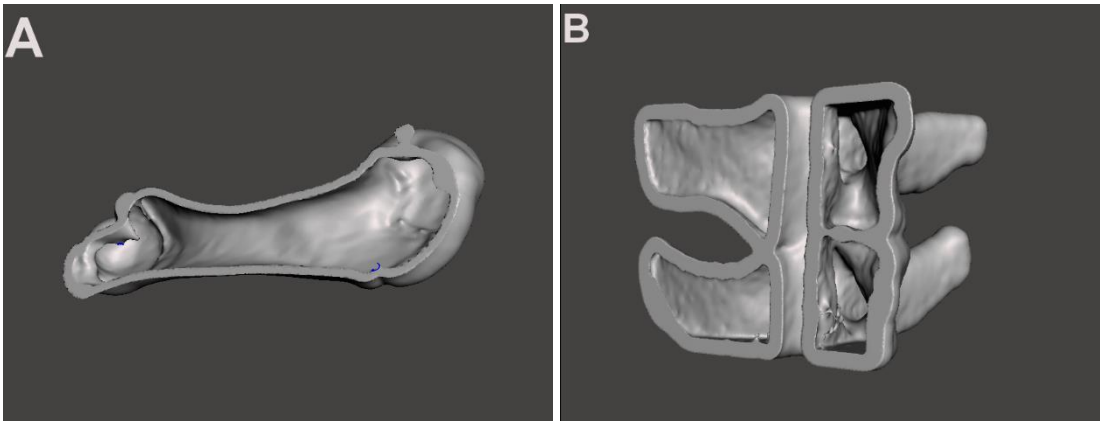

Figure 4: Moulds of porcine femur (A) and spine (B) ready for printing.

The moulds were printed on a 3D printer (Ultimaker 3 Extended; Ultimaker, Geldermalsen, The Netherlands) with blue polylactide (PLA) filament and polyvinyl alcohol (PVA) filament as

supporting material (both Ultimaker, Geldermalsen, The Netherlands). Surface irregularities of the printed mould were smoothed using sandpaper.

Before casting, a separating agent was applied on the moulds inner surface. Next, castable polyurethane (Aptflex F36, Precision Acoustics Ltd, Dorchester, United Kingdom) was prepared and poured into the mould. The material was cured for 6 hours at 70 °C.

The mould was afterwards removed from the hardened polyurethane. To this end, the mould was heated with a heat gun until the PLA turned soft and could be removed with tweezers in small steps.

The final model was encased into polyacrylamide (Figure 5) which was prepared as described above. Tissue mimicking attenuation was induced by adding 2% (w/v) silica particles (Sigma-Aldrich Corporation, St. Louis, Missouri, USA) before polymerization. The distance to the surface of the gel was equal to the beforehand on the CT scan measured distance from the skin to the treated area (facet joint, lateral part of corpus femoris).

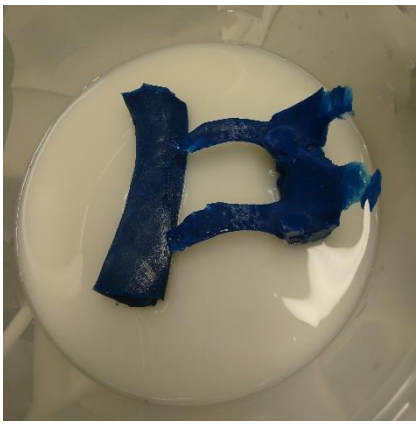

Figure 5: 3D models of porcine spine and femur in tissue mimicking gel.

An overview over the whole manufacturing process can be found in Figure 6.

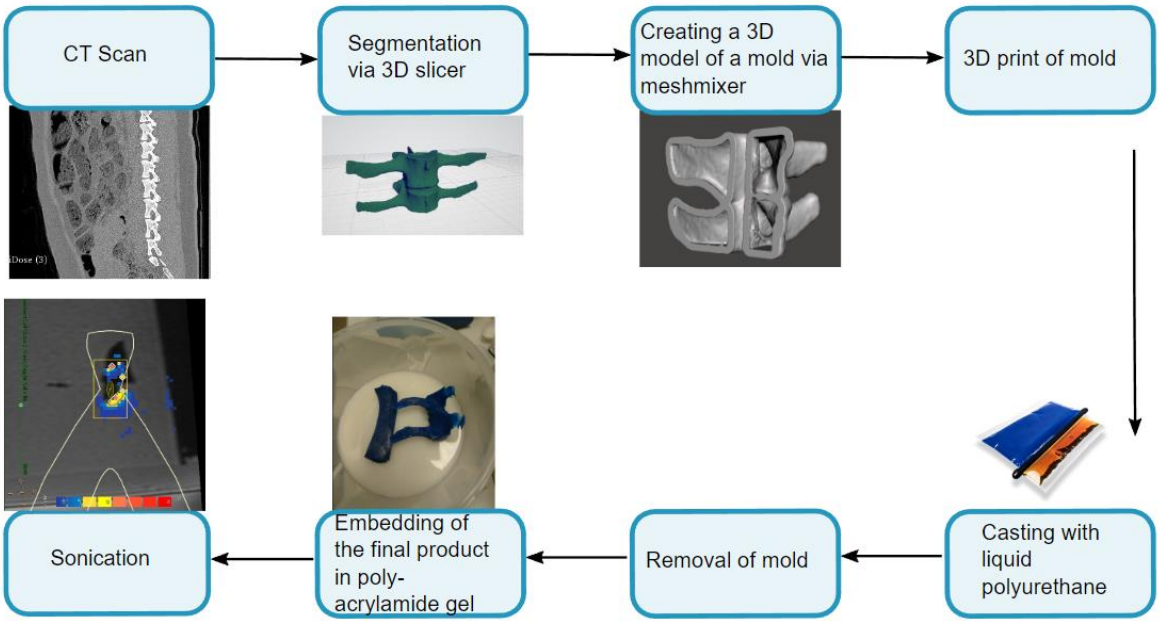

Figure 6: Workflow of the manufacturing process.

3.3.2. Alternative way of manufacturing

The method of producing a 3D phantom described above is feasible but takes a long time and especially the removal of the PLA is not convenient if one wants to produce a larger number of phantoms. For that reason, an alternative, more practical way of producing a phantom was developed (Figure 7).

Segmentation of the CT-scans of pigs was done as described in the first manufacturing method. The resulting 3D model was then exported as an STL file and printed on a Ultimaker 3 with PLA and polyvinyl alcohol PVA as supporting material. Based on the printed model a two-part silicone mould was created. Complex models like a facet joint were prepared by filling all holes like e.g., the spinal canal with candlewax. Otherwise, the model would not be removable from the silicone anymore.

The silicone mixture was prepared by mixing 500 ml HS620 silicone, 4% catalyst and 0.4% bubble free solution (Versandhandel Blioch, Ahrensburg, Germany).

The liquid silicone was poured in two steps: The first part of the silicone mould filled the spine model up to the processus spinosus, the second part covered the rest of the model up to the processus transversus. In the femur model, the first portion of silicone filled the model up to half of the height of the femur. The division into two pouring steps served as a breaking point for an easier removal of the printed model.

After the silicone mould was dried (2-3 hours at room temperature), the printed spine model was removed by separating the silicone at the border of the two pouring steps. The silicone mould reassembled and secured tightly with elastic bands. A mixture of liquid polyurethane (Aptflex F36) was prepared and poured into the mould. Curing took 24 hours at 40 °C in a vacuum drying oven. Due to the flexible nature of the silicone, removal of the final phantom was done by simply pulling.

This phantom could be used in the same way as the phantom created by the original approach.

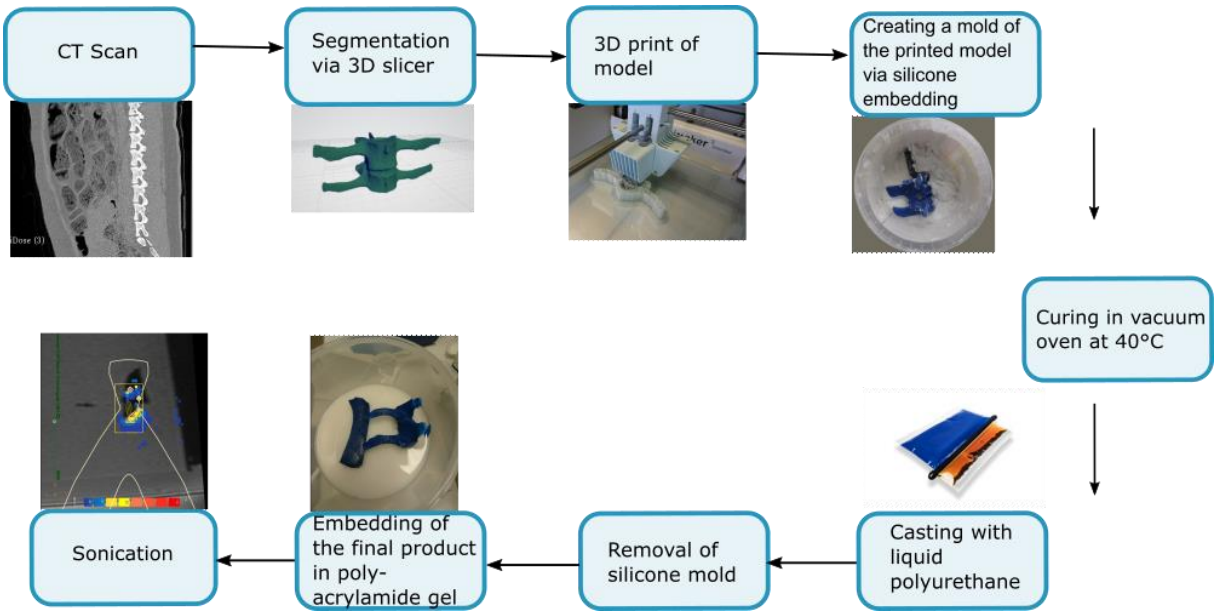

Figure 7: Workflow of the alternative way of manufacturing.

3.4 Experimental setup

All sonications were performed on a commercially available Sonalleve® V2 MR-HIFU system (Profound Medical Corp, Mississauga, Canada) with a 3.0 T MR scanner (Achieva®, Philips Healthcare, Best, The Netherlands). Before positioning the phantom on the HIFU table, a thin layer of degassed water was applied to the table's acoustic window. The phantom was placed with the open side of the plastic container downwards in the middle of the HIFU window. To ensure reproducible positioning of the phantom, a customized positioning plate was used to hold the phantom in the middle of the window (Figure 8).

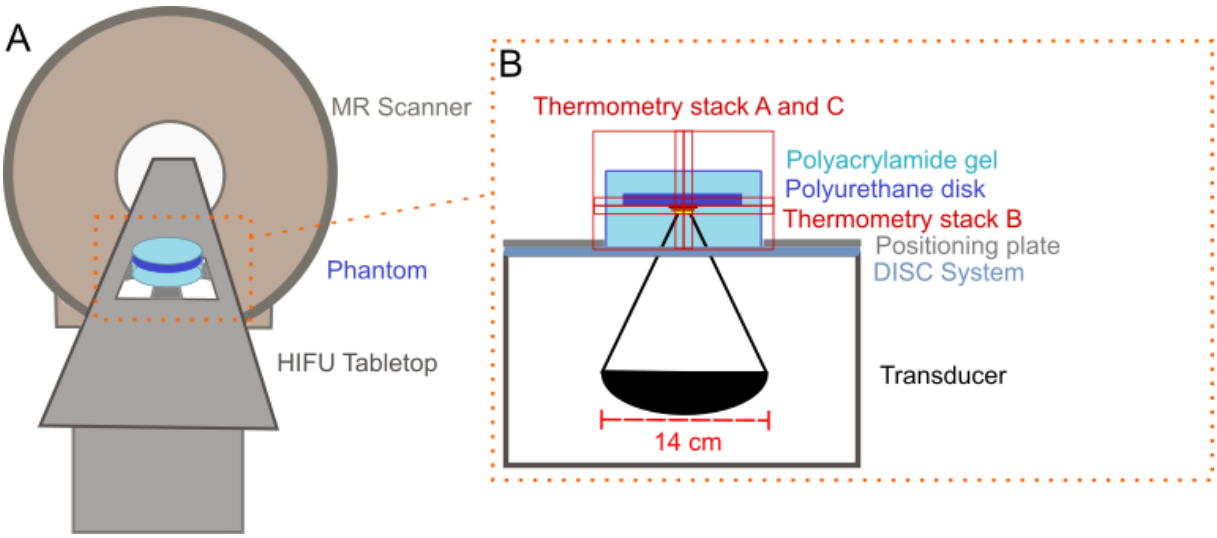

Figure 8: Schematic model of the experimental setup, A: Front view of the whole setup with HIFU tabletop, phantom and MR scanner, B: Close up of the HIFU transducer.

The sonications were planned using 3D T_1 weighted turbo field echo scan (Figure 9). A balanced fast gradient echo sequence was acquired right after the planning scan to detect bubbles present at interfaces (termed "Bubble scan"). Thermometry was performed using the proton resonance frequency shift (PRFS) method.[45] The employed MRI sequence was an RF-spoiled gradient echo sequence with 4 slices in total: 2 slices parallel to the beam (sagittal and coronal plane) and 2 coronal slices perpendicular to the beam (T_R = 25.17 ms, T_E = 16 ms, voxel volume = 2.083 × 2.083 × 7.0 mm^3, flip angle FA = 18°, dynamic scan time = 3.25 s).

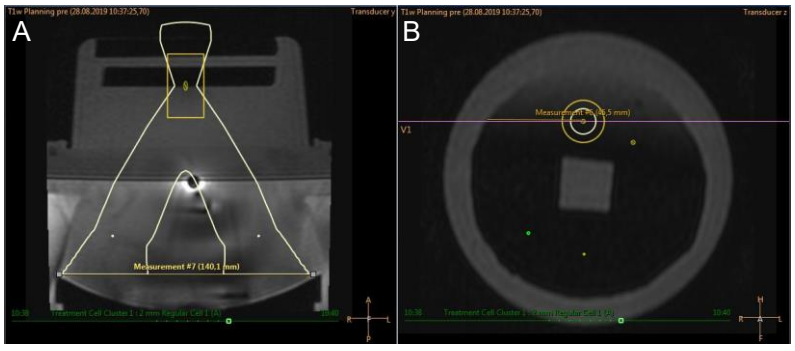

Figure 9: A: Frontal and B: transversal slice of the T1 planning scans.

3.5 Analysis of experiments

3.5.1. Temperature measurement in reproducibility and power dependence investigations

As part of the thesis, a software tool was programmed in python (version 2.7.15)[122] for analysis of the temperature maps that were acquired with PRFS thermometry during sonication. As MR-based thermometry is impossible inside the phantom material due to too short T_2 and lack of water protons, temperature changes were accessed in the adjacent polyacrylamide gel. The region of interest (ROI) was placed automatically in a distance of 4 mm to the phantom surface to avoid any partial volume effects (Figure 10). The size of the ROI for temperature readout was chosen such that the entire heated region including voxels heated by diffusion was captured. The ROI's diameter was 6 mm in 2 mm sonication volumes, 12 mm in 8 mm sonication volumes, 16 mm in 12 mm sonication volumes and 20 mm in 16 mm sonication volumes. Exact placement of the ROI was ensured by determining the middle of the focal spot using a gauss function fit (lmfit package, version 0.9.13[123]) of the temperature distribution in a ROI parallel to the surface of the absorber. The centre of the gauss function was used as a reference for the middle of the ROI.

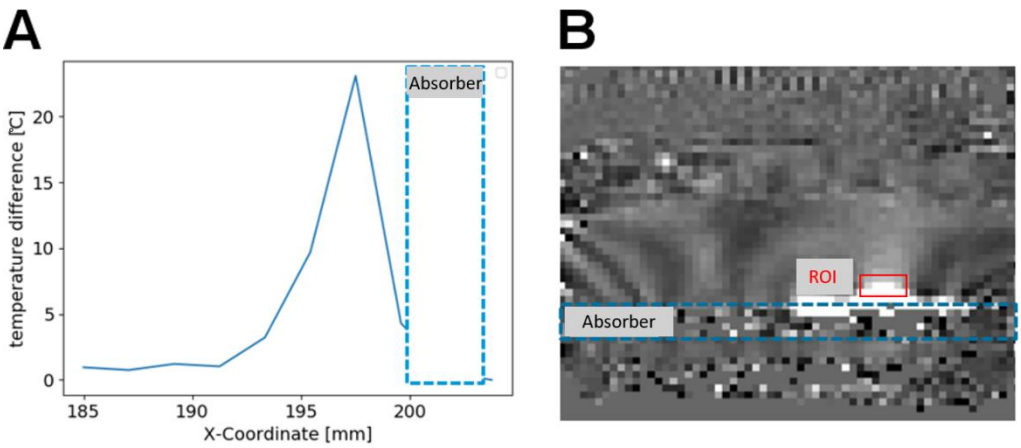

Figure 10: A Temperature profile perpendicular to the absorber: B: placement of the ROI in python program.

3.5.2. Thermal dose calculation in the comparison of indirect/ direct approach and equal energy comparison

The thermal dose was calculated according to the following equation [20,124]

$$CEM43 = \sum_{k=0}^{k_N} R^{(43-T_k)} * \Delta t$$
$$R = \begin{cases} 0.233, & T_k < 43\ °C \\ 0.428, & T_k \geq 43\ °C \end{cases} \quad (6)$$

with the temperature T_k at the timestep k, the timestep size Δt, and the dose rate constant R.

Due to the limited resolution of the MR thermometry images, the volume V, which accumulated for a CEM43 value of more than 240 min, was approximated as half of a spheroid (Figure 11):

$$V = \frac{4}{6} * \pi * r^2 * h \tag{7}$$

with the radius r and the height h. The radius and height were determined by the average distance over a CEM43 value of 240 min from sagittal and transverse temperature monitoring slices. Measurements were performed with the software ImageJ.[125]

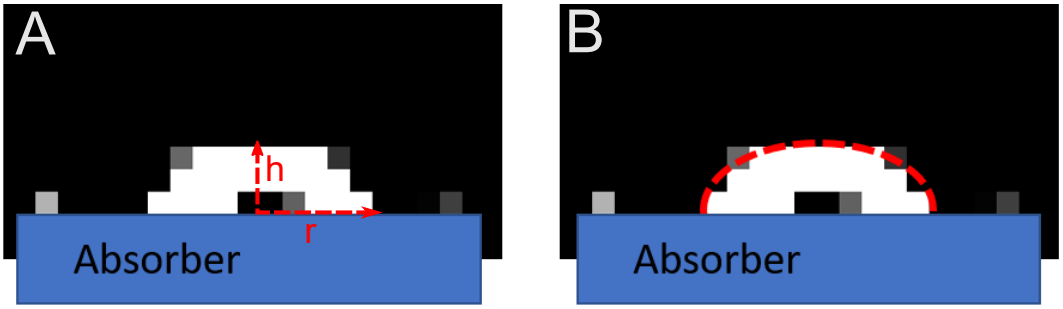

Figure 11: Native CEM43 maps (white) of the sagittal slice after a sonication. A: Radius r and height h are measured; B: Approximation of the half spheroid.

3.5.3. Statistical analysis

All statistical tests were performed using custom scripts written in Python 2.7.[122] Further information on statistical tests and used packages can be found in the appendix.

4. Results

4.1 Identification of bone phantom material

Several materials such as PMMA, PC, Verowhite and polyurethane were embedded in polyacrylamide and tested for their properties to serve as a bone phantom material. After sonication, the material was examined for damage. While PMMA, PC and Verowhite showed clear damage after sonication (Figure 12), polyurethane showed no visible damage (Figure 13) and qualified for the next step of manufacturing. In all further experiments, polyurethane is used as bone phantom material, and any reference to “phantom” implies the usage of polyurethane embedded into a polyacrylamide gel.

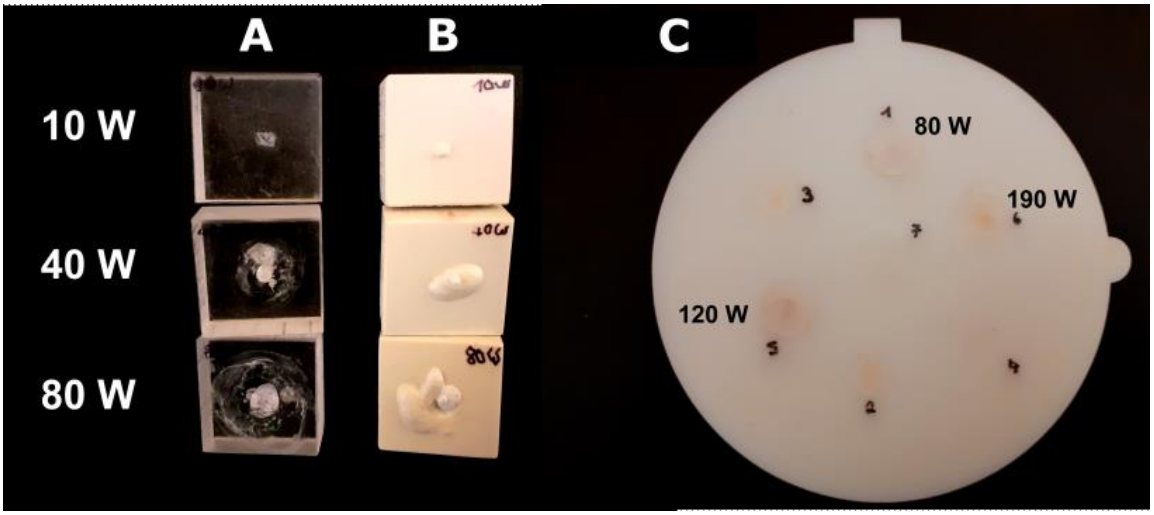

Figure 12: Various materials after MR-HIFU sonications with a power of 10, 40 and 80 W or 80, 120 and 190 W. Sonication time was 16 s. A: Polymethylmethacrylate (PMMA), B: Polycarbonate (PC) and C: Verowhite.

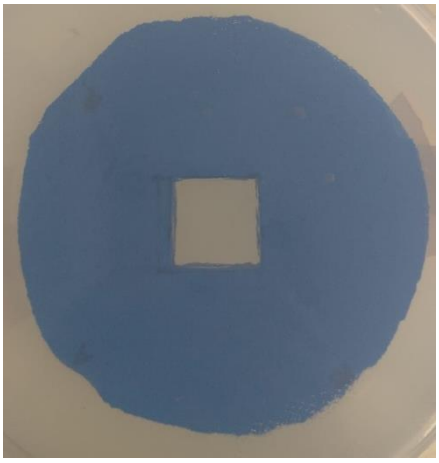

Figure 13: Polyurethane inside the polyacrylamide gel after a sonication session without any visible signs of heat damage.

4.2 Reproducibility

For testing the reproducibility of heating, 20 sonications (40 W, 20 s, Figure 14) using an 8 mm cell were repeated on different days over a period of 11 weeks. At each session, three sonications were performed at different locations of the phantom. The polyacrylamide gel was changed once and recreated after the exact same recipe. The temperature evolution during each sonication was tracked using MR-thermometry, analysed as described (materials and methods, appendix) and compared. Figure 15 shows the maximum (T_{max}) and average temperature (T_{mean}) in the ROI placed in the polyacrylamide gel adjacent to the bone phantom as a function of sonication time. For used sonication parameters, T_{max} in the predefined ROI increases with 0.58 ± 0.02 °C/s, while the T_{mean} increases with 0.23 ± 0.01 °C/s (Table 2), which leads to a temperature difference of 12.08 °C and 4.79 °C at the end of the sonication (after 19.4 s).

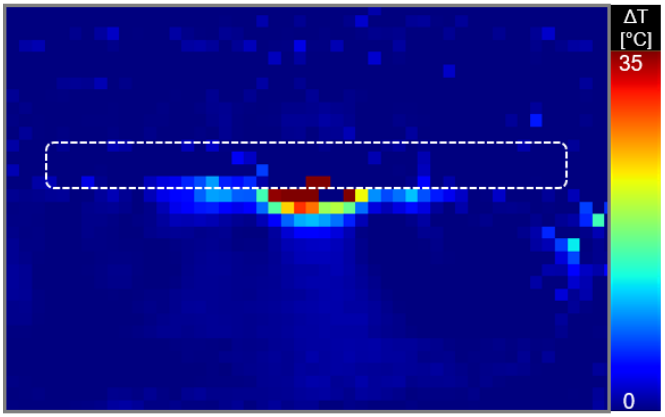

Figure 14: Representative temperature map of a sonication used for the reproducibility test. Temperature data was acquired after 20 seconds of sonication with 40 W in an 8 mm sonication volume. The dashed white line indicates the position of the absorber.

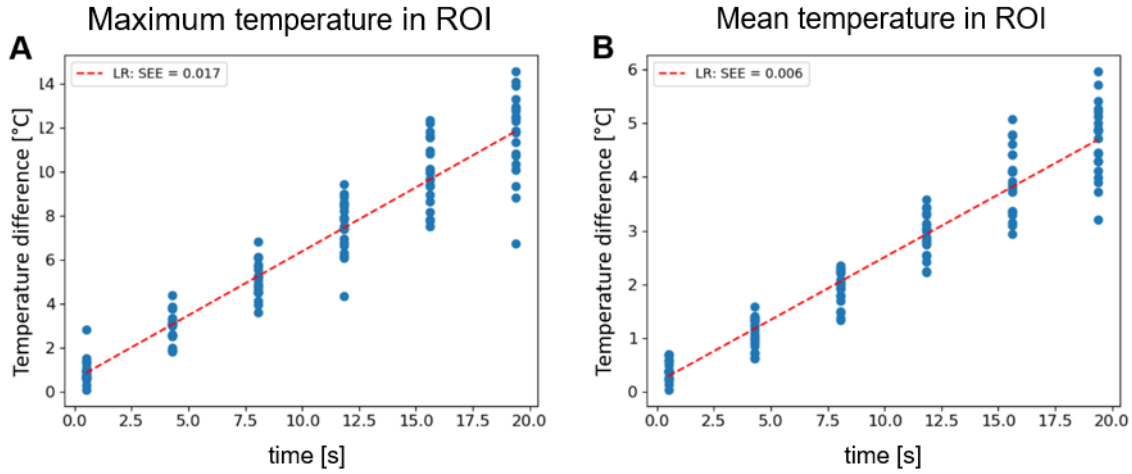

Figure 15: A: Maximum and B: mean temperature evolution in a defined ROI in 4 mm distance to the absorber (8 mm sonication volume, 40 W, 20 s sonication time, n= 20).

Table 2: Result of the linear regressions performed on the temperature measurement in an 8 mm sonication volume with a power of 40 W over 20 s.

	Temperature slope [°C/s]	**SE [°C/s]**	**Intercept [°C]**	**p-value**	**R^2**
T_{mean} in ROI	0.23	0.006	0.19	<0.001	0.918
T_{max} in ROI	0.58	0.017	0.55	<0.001	0.907

The residuals were calculated to quantify the scattering of the individual measurement points from the expected values. A linear regression over all measurement points served as a basis for the expected values. R^2-values for the linear regression were 0.918 for T_{max} and 0.907 for T_{mean} in the ROI. The values of the residuals range from -5.09 °C to 2.72 °C in the heating curve of T_{max} and from -1.49 °C to 1.26 °C in the heating curve of T_{mean} (Figure 16).

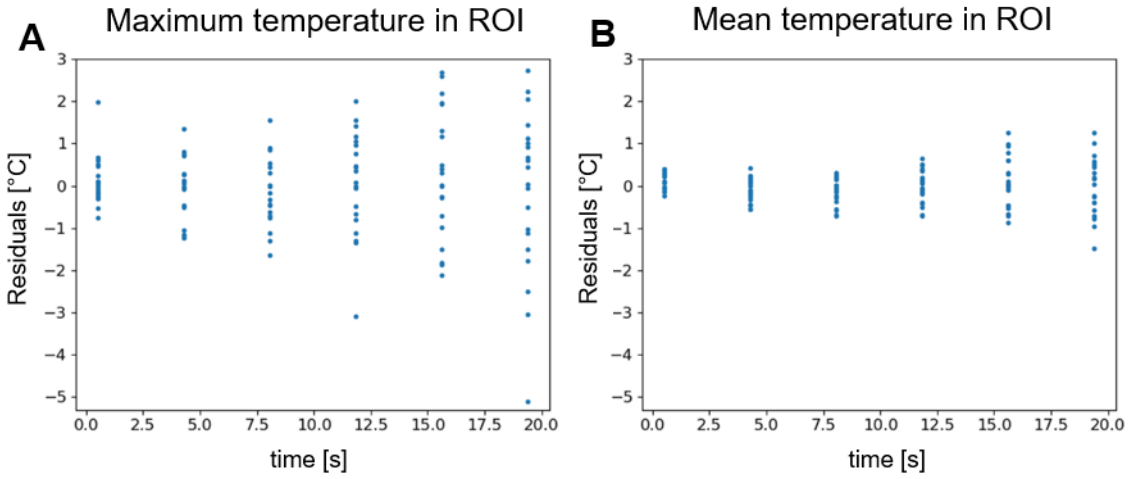

Figure 16: Residuals of the single temperature measurements calculated from the linear regression of all temperature measurements. A: residuals from maximum temperature evolution in the ROI, B: residuals from mean temperature evolution in the ROI.

A linear regression of the temperature values over the time span in which the experiments were conducted showed a slope value of -0.023 °C/d for T_{max} values and a slope value of -0.008°C/d for T_{mean} values (Figure 17).

The slope values of a linear fit of the temperature increase over time in the single sonications range from 0.36 °C/s to 0. 73 °C/s (Figure 18). The slope values of repeated sonications for T_{max} and T_{mean} performed at a single day remain comparable over the entire period of the experiments and do not significantly changing with age of the phantom.

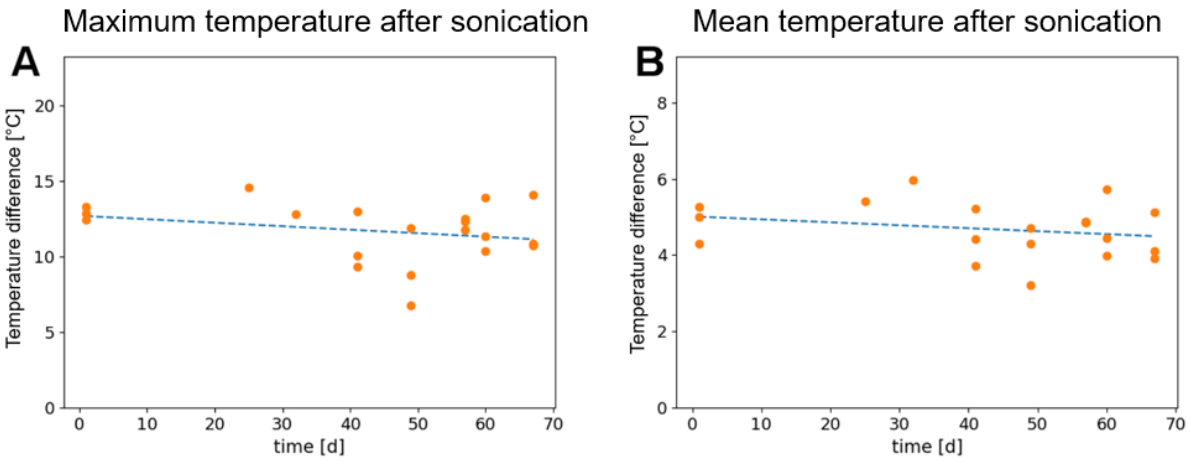

Figure 17: Repeated measurement of temperature (A: T_{max}, B: T_{mean} in a defined ROI) at the end of the sonication (8 mm sonication volume, 40 W, 20 s sonication time) over a period of 66 days.

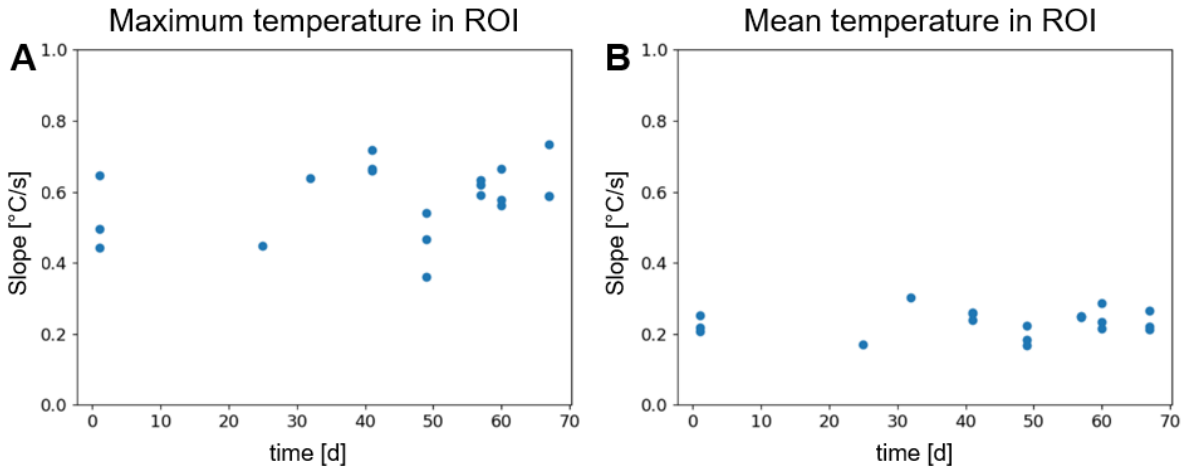

Figure 18: Slope values of a linear regression of repeated sonications (8 mm sonication volume, 40 W, 20 s sonication time) over a period of 66 days. A represents T_{max}, B T_{mean} values in a defined ROI.

4.3 Power dependence

To investigate the effect of different power settings, two sets of sonications using a 2 mm cell (2 mm diameter, 7 mm length) with 20, 40, 60 and 80 W were performed for 16 s (Figure 19). Temperature evolution during each sonication was tracked using MR-thermometry as described above and compared.

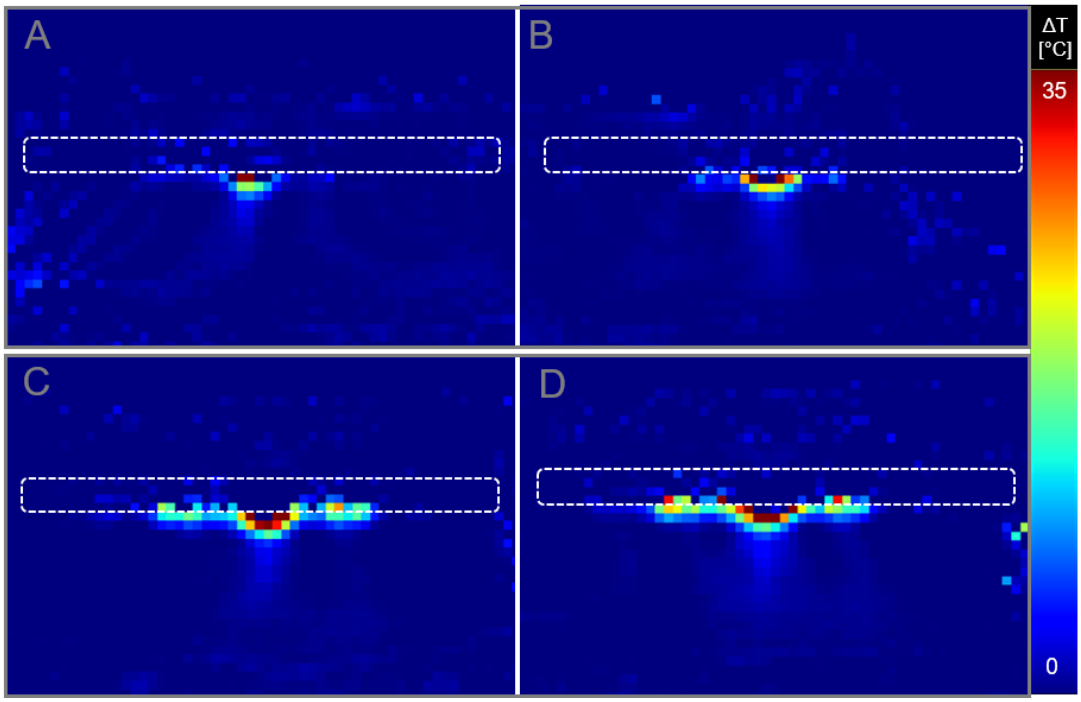

Figure 19: Representative temperature map of sonications in a 2 mm sonication volume with A: 20 W, B: 40 W, C: 60 W and D: 80 W. Temperature data was acquired after a sonication duration of 16 s. The dashed white line indicates the position of the absorber.

Increasing power led to T_{max} slope values from an average 0.82 °C/s in sonications with 20 W, 0.98 °C/s in sonications with 40 W, 1.13 °C/s in sonications with 60 W and 1.36 °C/s in sonications with 80 W. For T_{mean}, slope values ranged from 0.46 °C/s (20 W sonication power) to 0.92 °C/s (80 W sonication power) (Table 3, Figure 20). A fit of the T_{max} slope values over power resulted in a slope value $8.8 \cdot 10^{-3}$ °C/s/W (correlation coefficient $R^2 = 0.966$, Figure 21). The same fit for T_{mean} slope values led to a slope value of $7.3 \cdot 10^{-3}$ °C/s/w (correlation coefficient $R^2 = 0.979$).

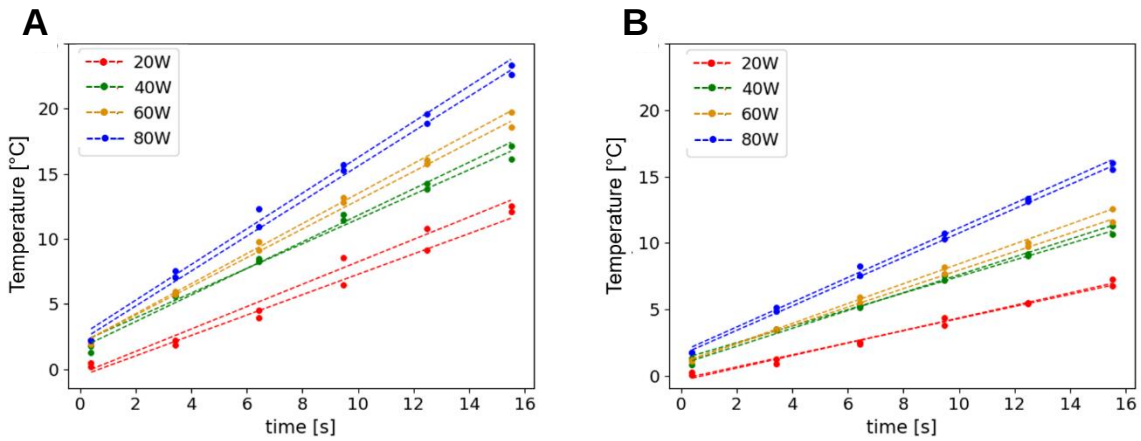

Figure 20: Temperature increase (A: T_{max}, B T_{mean} in a defined ROI) over time for the four different power settings (n = 2 for each power setting). Blue = 80 W, orange = 60 W, green = 40 W and red = 20 W sonication power. All sonications were performed in a 2 mm sonication cell with a sonication duration of 16 s.

Table 3: Average slope values of a linear fit of the maximum and mean temperature increase over the sonication time of 16 s for the four different power settings.

Sonication power [W]	20	40	60	80
Average slope value of T_{max} in ROI [°C/s]	0.82	0.98	1.13	1.36
Average slope value of T_{mean} in ROI [°C/s]	0.46	0.65	0.72	0.92

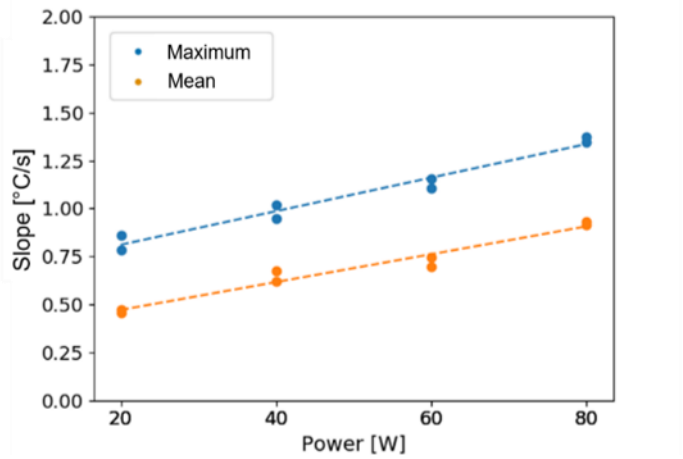

Figure 21: T_{max} (blue) and T_{mean} (orange) slope values of the linear temperature increase over time for the four power settings (20, 40, 60 and 80 W). The dashed line indicates a linear fit of the slope values over power.

4.4 Equal energy comparison

Six sonications with the same energy (800 J) were performed in one session: three at a power of 40 W for 20 s, three at a power of 20 W for 40 s. A post sonication time of 5 minutes was monitored via thermometry to enable the calculation of the thermal dose after cooldown.

The sonications with less power and longer time led to a mean volume heated over a CEM43 value ≥ 240 min of 2.16± 0.25 ml. The sonications with higher power and shorter sonication time led to a mean volume heated over a CEM43 value ≥ 240 min of 2.44 ± 0.44 ml (Figure 22). The difference between the mean volume of both sonication protocols was found to be 0.28 ml. A two sided independent-samples t-test showed no significant difference between the two sonication approaches (p-value = 0.481). These sonications with the same total energy, but different power and time settings lead to comparable volumes having a CEM43 value ≥ 240 min (Figure 24).

The temperature slopes of the two sonication settings showed differences: In the sonications with more power and less time a steeper rise of the temperature was observed than in the sonications with less power and more time (Figure 23).

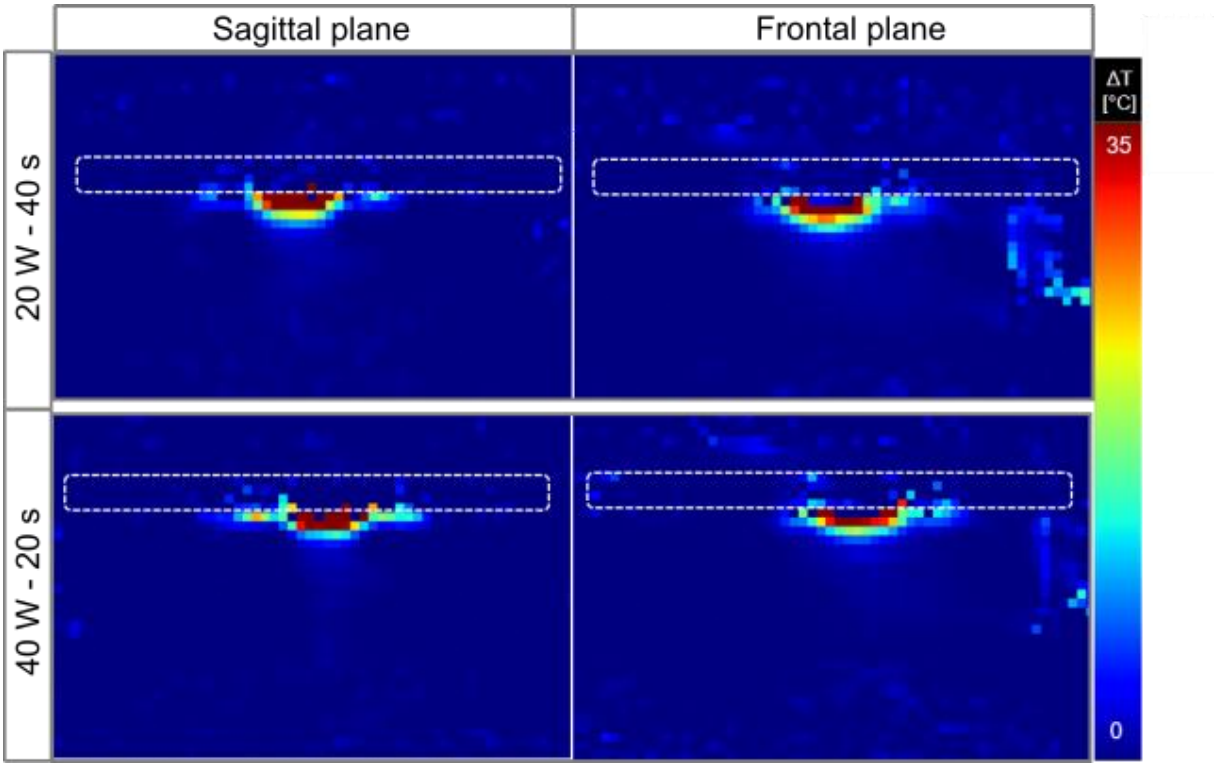

Figure 22: Representative temperature map of a sonication with 20 W for 40 s, captured after 43 s and a sonication with 40 W for 20 s, captured after 21,5 s. The dashed white line indicates the absorber.

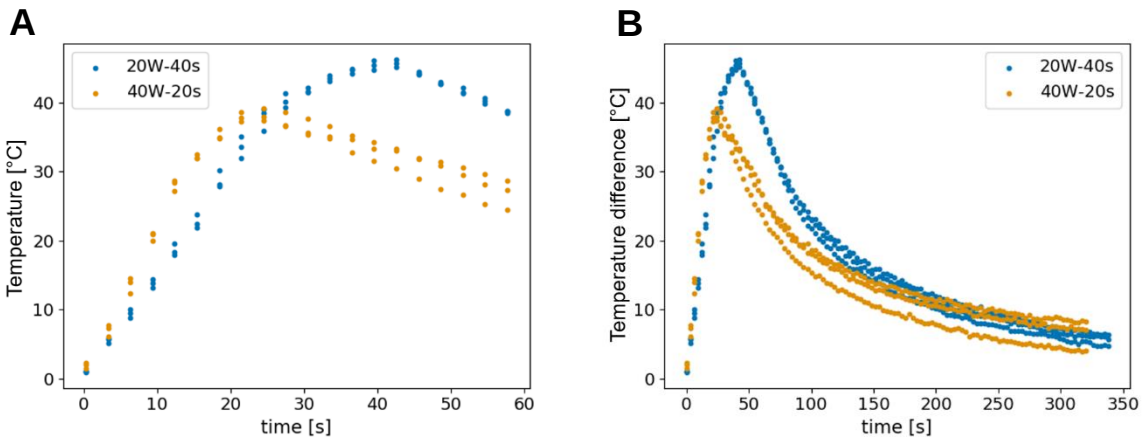

Figure 23: Heating curve over time for the two sonication protocols (blue: 20 W power, 40 s sonication time; orange: 40W power, 20 s sonication time). Temperature values represent the hottest voxel in the predefined ROI. A: showing the initial rise of temperature, B: showing broader timespan including cool-down.

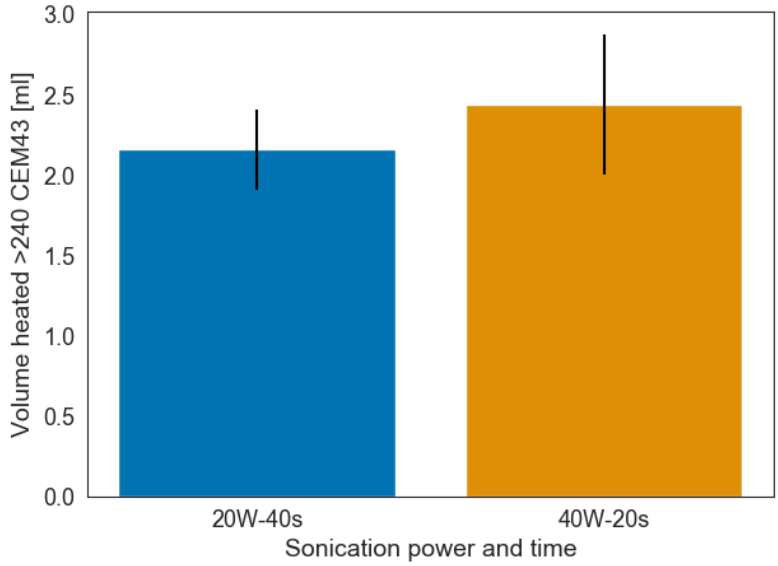

Figure 24: Volumes exceeding a thermal dose (CEM43) of 240 min (n=3 for each approach) after sonications with a sonication energy of 800 J, but different power and durations (20 W and 40 s vs 40 W and 20 s). Error bars indicate the standard deviation.

4.5 Indirect/ direct approach comparison

For the direct approach, target volumes of 8-, 12-, and 16- mm in diameter were defined directly on the absorber's surface. For the indirect approach, target volumes of 2 mm in diameter were defined in a distance to the surface of the absorber calculated by the intercept theorem (Figure 25). In theory, this leads to the same heated area as in the direct approach. All sonications were performed with a power of 40 W and repeated 3 times in the same MR-HIFU session (Table 4). Post sonication temperature measurements were performed for 5 minutes to enable the calculation of the final thermal dose after cooldown.

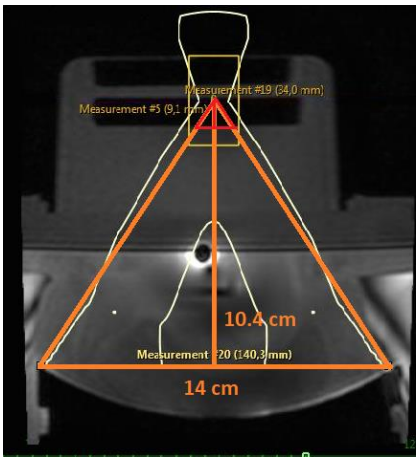

Figure 25: Calculation of the heated area at the surface of the phantom with the indirect sonication approach.

Table 4: Sonication parameters of the direct/ indirect approach.

Diameter (mm) of planned ablated area on the surface of the phantom	Approach	Distance of the focal spot to absorber surface (mm)	Cell size in MR-HIFU console (mm)	Sonication duration (s)
8	Direct	0	8	20
	Indirect	6	2	20
12	Direct	0	12	36
	Indirect	9	2	36
16	Direct	0	16	56
	Indirect	12	2	56

The indirect and direct sonication approach led to a comparable volume heated over a CEM43 value ≥ 240 min (Figure 26 and 29, Table 5) for all of the tested target volumes.

The temperature rise during the sonication was slightly steeper for the indirect approach in the 8- and 12 mm treatment volume, however this finding was not consistent for the 16 mm treatment volume where the direct approach showed a steeper rise (Figure 27 and 28).

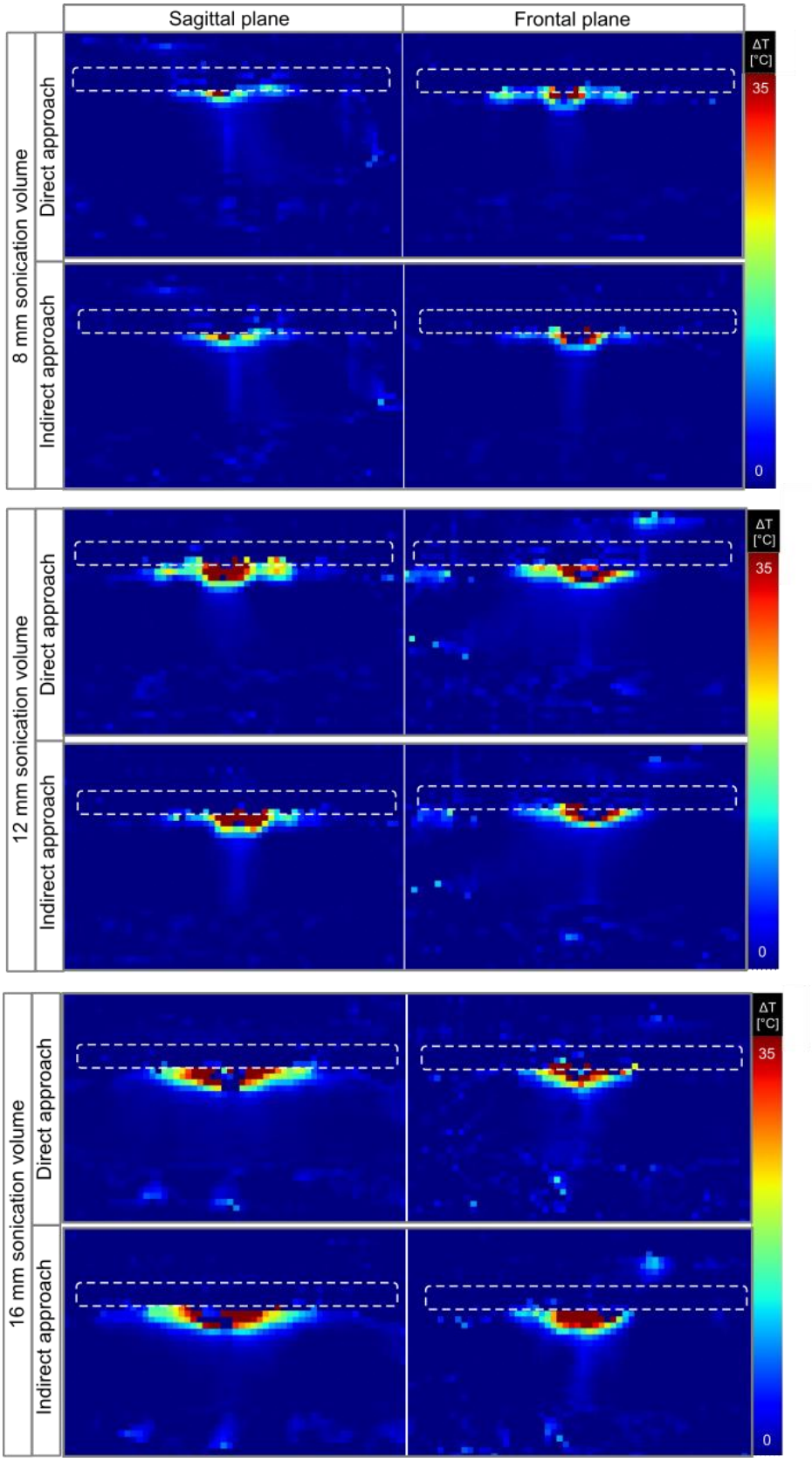

Figure 26: Temperature maps comparing the direct approach vs. the indirect approach in different treatment volumes from 8 to 16 mm diameter. Temperature maps were acquired after 22 s (8 mm sonication volume), 37 s (12 mm sonication volume) and 58 s (16 mm sonication volume) sonication time. The dashed white line indicates the position of the absorber.

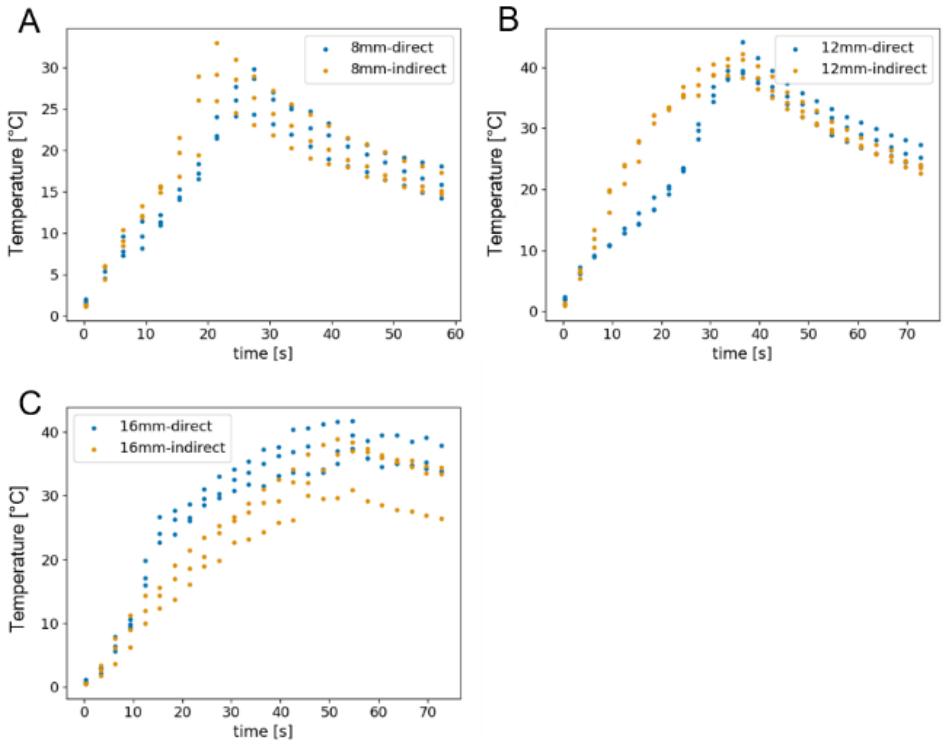

Figure 27: Maximum temperature difference from baseline over time in the specific sonication volumes (A: 8 mm, B: 12 mm, C: 16 mm) comparing the indirect (orange) and direct (blue) approach. The graph shows the temperature rise during the sonication and shortly after the end of sonication.

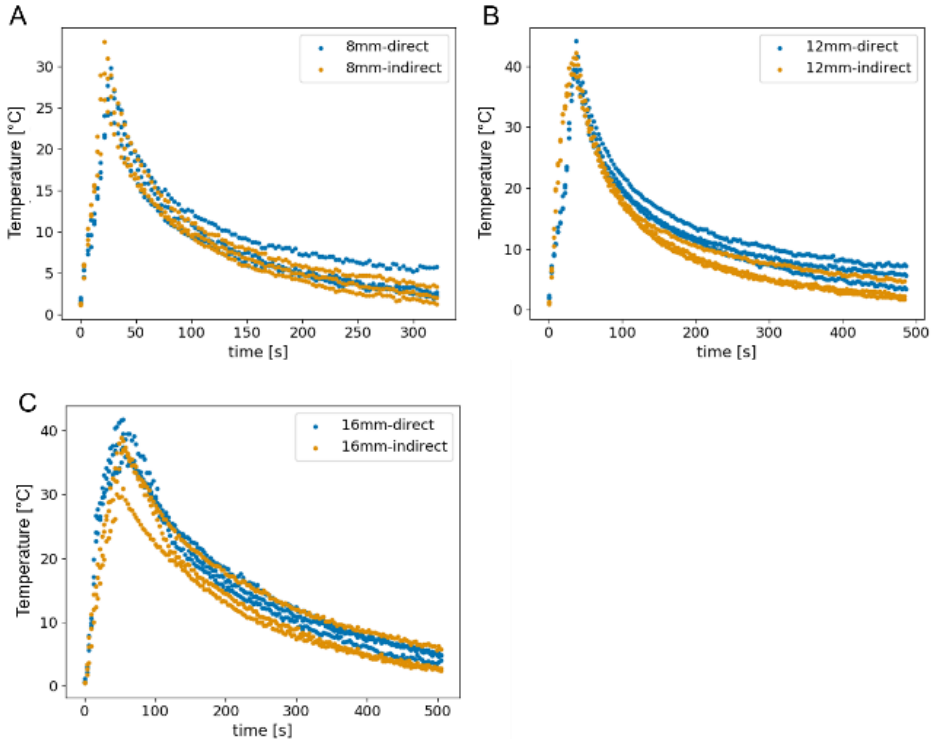

Figure 28: Maximum temperature difference from baseline over time in the specific sonication volumes (A: 8 mm, B: 12 mm, C: 16 mm) comparing the indirect (orange) and direct (blue) approach. The graph shows the temperature rise during the sonication and the full post sonication time.

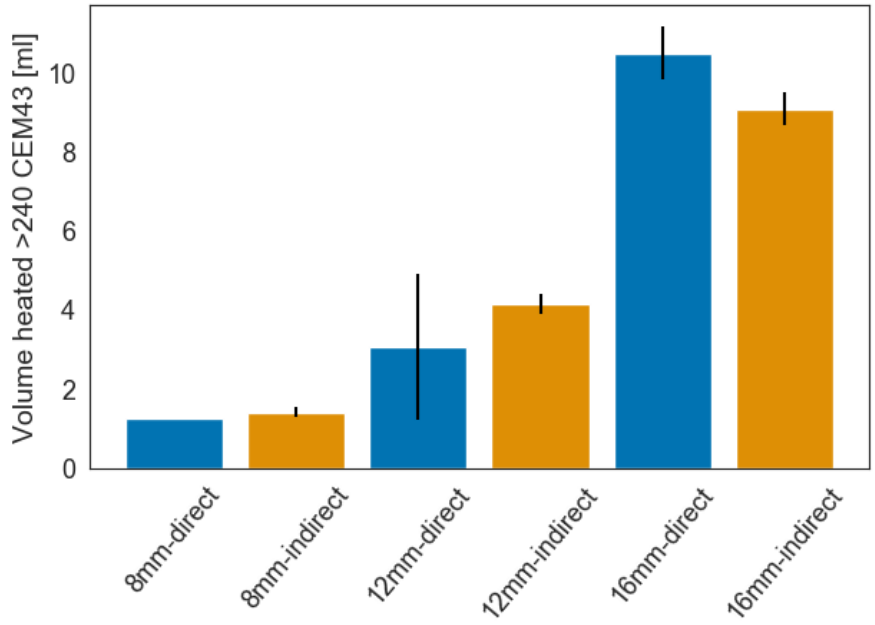

Figure 29: Comparable ablated volume (CEM43 value ≥ 240 min) in direct and indirect approach. Target volumes from 8 to 16 mm diameter were used (n=3 for each cell size and approach). Error bars indicate the standard deviation.

*Table 5: Mean volumes and difference between the mean volumes of 8-, 12- and 16-mm target volumes in direct and indirect approach (n=3 for each cell size and approach). P-value is calculated from the paired-samples t-test comparing indirect and direct approach. *No standard deviation, since all values were exactly the same*

	8mm-direct	**8mm-indirect**	**12mm-direct**	**12mm-indirect**	**16mm-direct**	**16mm-indirect**
Mean volume [ml]	1.28±0	1.43± 0.110	3.081± 1.835	4.157± 0.264	10.513± 0.654	9.1± 0.410
Difference between mean volumes [ml]	0.148		1.08		1.43	

4.6 Sonications performed with a Spine Phantom

4 mm sonication volumes were placed directly on the facet joint of the spine phantom according to a previously performed in-vivo swine experiment. Sonication powers of 100 and 120 W were used for 16 s. The experiments were analysed in terms of the maximum temperature difference from the baseline room temperature reached during the sonication. The temperature was measured in the gel surrounding the facet joint.

In the sonication with 100 W for 16 s (1600 J) the maximum temperature difference was 39.5 °C and 42.8 °C in the sonication with 120 W for 16 s (1920 J) (Figure 30 and 31).

The in-vivo swine experiment showed a peak temperature difference from body temperature (37°C) of 24.9 °C in the treatment with 100 W for 16 s (1600 J) and a peak temperature difference of 26.4 °C in the treatment with 120W for 16 s (1920 J).

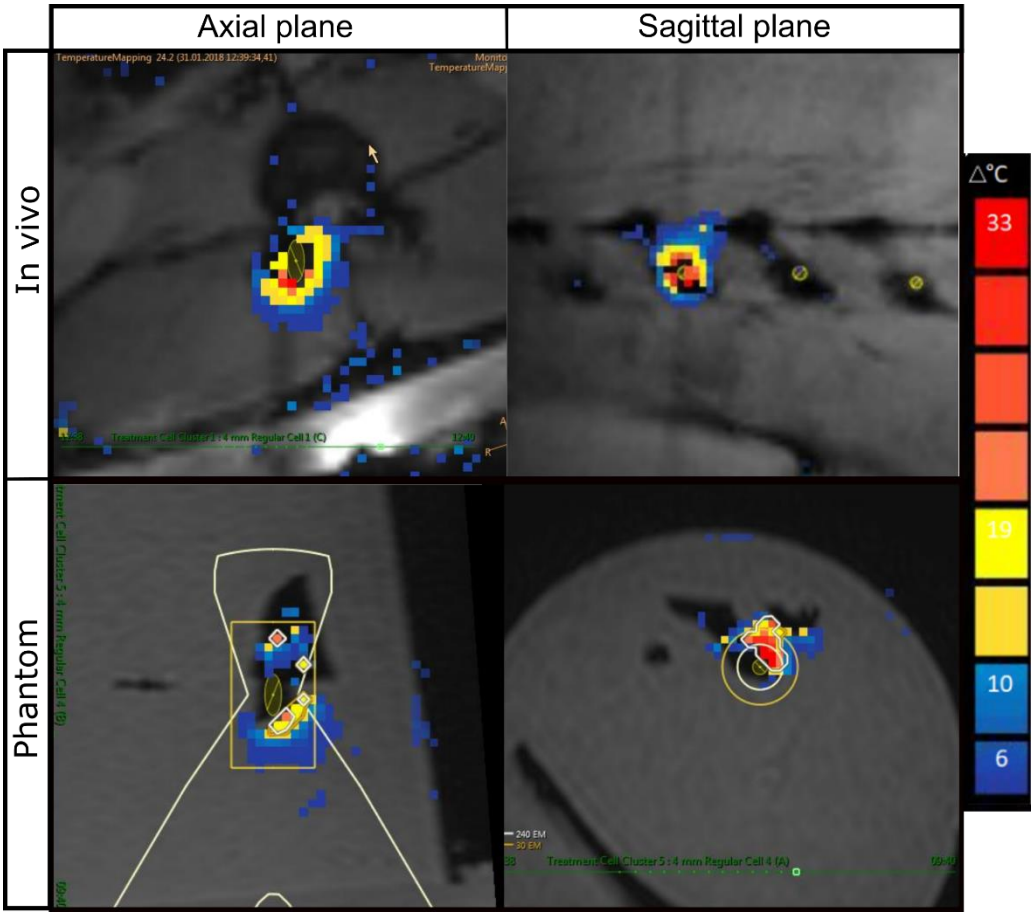

Figure 30: Temperature map of the pig facet joint treatment and of the spine model treatment. Each treatment was accomplished with 4 mm sonication volumes, 100 W power and 16 s sonication duration.

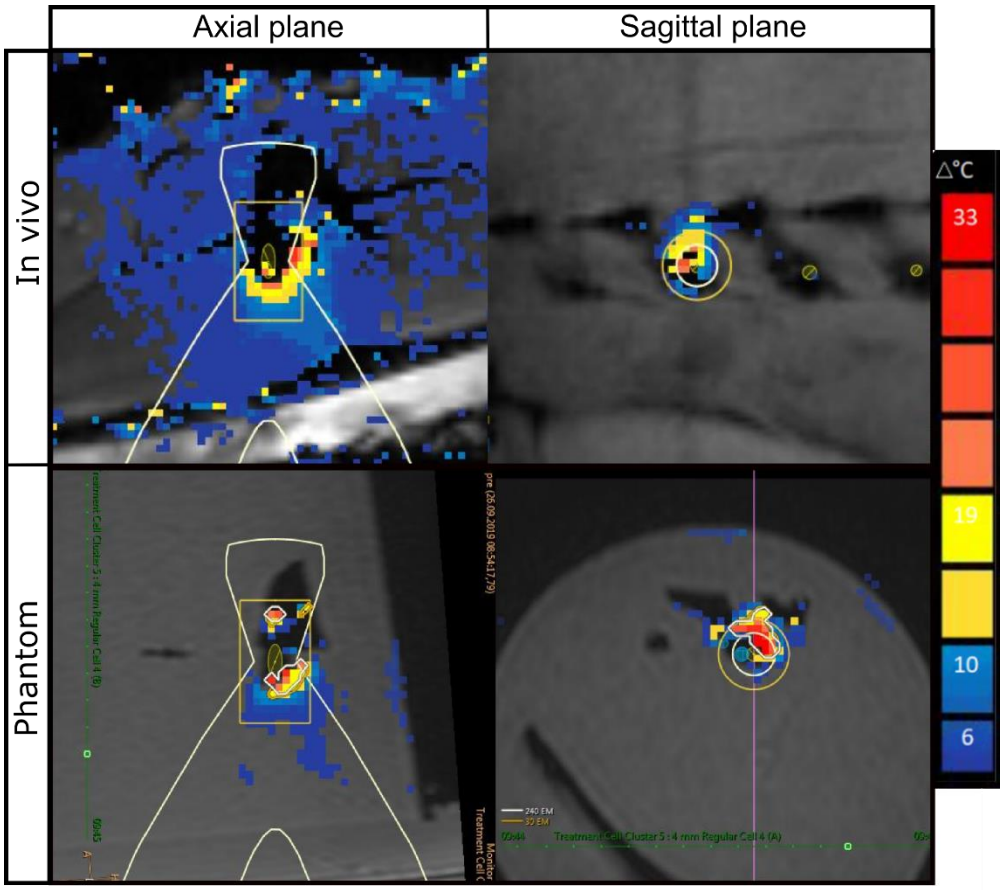

Figure 31: Temperature map of the pig facet joint treatment and of the spine model treatment. Each treatment was accomplished with 4 mm sonication volumes, 120 W power and 16 s sonication duration.

5. Discussion

The study demonstrates that the developed bone phantom consisting of a flat disk of polyurethane embedded in a polyacrylamide gel is a reliable tool to test different MR-HIFU systems as well as sonication protocols. In contrast to other tested materials such as PMMA, Polycarbonate and Verowhite, only polyurethane did not degrade after repeated exposure to HIFU. The polyurethane phantom could be used over a considerable amount of time and showed a reproducible temperature rise for repeated sonications with the same settings. Our bone phantom could therefore be used for quality assurance and testing of MR-HIFU sonication protocols in the context of bone applications. To our knowledge, such a phantom has not yet been described in literature. Furthermore, we characterized the quality assurance phantom regarding exposure to different power levels and different sonication approaches for bone treatment. In addition to the quality assurance phantom, a realistic bone model of the facet joint was developed.

Out of all the materials we tested as a candidate for the bone phantom, polyurethane was the best choice regarding durability and resistance to heat. Other materials we tested like verowhite as the standard 3D-printing material or cheaper plastic options such as polycarbonate or PMMA turned out to be instable and showed signs of degradation under MR-HIFU exposure.

Besides durability, one important feature of the bone phantom is that it leads to a reproducible temperature rise. We investigated this quality by measuring the temperature rise during a specific sonication in a defined ROI. This sonication was repeated during multiple experiments over the timespan of eleven weeks. The maximum (T_{max}) and mean temperature (T_{mean}) in the defined ROI were determined.

The value of T_{mean} averaged over the entire volume is always lower than T_{max} close to the position of the focal spot at the surface which acts as the heat source. The adjacent gel is subsequently heated by heat diffusion into the gel leading to a lower T_{mean}. It should be taken into account, that perfusion may impact the value of T_{mean} more than T_{max} when sonications are performed in a patient setting.

To quantify the reproducibility of the bone phantom a linear regression of the temperature measurement over the sonication time was performed. R^2 values of 0.918 and 0.907 show a high correlation to the linear regression, which confirms our choice for this modelling approach. The resulting standard error of the estimated slope of $\Delta\, dT_{mean}/dt = \pm$ 0.006 °C/s (mean temperature analysis) and $\Delta\, dT_{max}/dt = \pm$ 0.017 °C/s (maximum temperature analysis) indicates an accurate prediction of the linear regression values and therefore a low variability of the measurements.

The variance of the measurement points was further characterized by calculating the residuals. We observed low residual values which means the repeated measurements were uniform. The

highest value for the residuals (ranging from -5.094 °C to 2.72 °C) were measured at the end of the sonication. The increasing difference from the residuals versus the fitted data points indicates heteroskedasticity. This phenomenon can be explained under the consideration that the difference of the slope values of the single sonications lead to a multiplying deviation with increasing time. The slope values of the single sonications ranged from 0.355 °C/s to 0. 733 °C/s. The difference in the slope values and residuals can be explained by a natural variation in heating, phantom positioning and also temperature readout (measurement error), since it is not possible to repeat an experiment in the exact same way.

The analysis of the influence of different power levels suggests a linear relation between applied power and temperature rise. As in the reproducibility experiments, the slope value of T_{mean} is always lower than T_{max}. With increasing power, the slope values of the temperature values (T_{max} as well as T_{mean}) over time showed a positive linear correlation with high correlation coefficients (0.966 and 0.979).

The results demonstrate that the increase of acoustic energy, i.e. increasing applied power while keeping sonication times constant has a linear impact on the maximum temperature reached in the focal spot. Changes in power settings therefore have an impact on the ablated volume and treatment duration. This underlines the demand for a standard on how to describe treatment settings in publications.

Sonications performed with an equal sonication energy (800 J), but different power and sonication times yield similar volumes with a CEM43 value >240 min. The heating rate and therefore the temperature at the bone phantom surface is proportional to the time-averaged acoustic intensity $I_{TA,}$ and the sonication time t, which as a consequence leads to the same temperature rise when the acoustic energy $E_{acoustic} = p_o^2 \cdot \Delta t$ is constant. In the experiments, the temperature change of the bone phantom is not measured directly but in the adjacent gel. Heat dissipation from the focal area (intersect of beam and bone phantom surface) is governed by diffusion into the bone phantom itself and into the gel where the heated area acts as a heat source after sonication is already stopped equilibrating over time. As the calculation of the CEM43 value >240 min integrates the entire temperatures over time, similar CEM43 values >240 min values are expected for the same applied acoustic energies. The experiments with a longer sonication time and less power showed a higher temperature peak and therefore presumably a slightly higher absolute CEM43 value, however the ablated volume remains similar for both sonication protocols. Note, that above may not hold in vivo, where perfusion of the tissue adjacent to the bone surface adds to heat dissipation.

At the end of the five minutes post-sonication temperature measurement temperature values still had not reached their baseline. This does not mean that the phantom is still warm, more likely the temperature measurement was impacted by the drift phenomena (there was no drift correction measurement in use).

We showed that the indirect treatment approach is comparable to the direct treatment approach when tested in-vitro on a phantom for small ablation volumes up to 16 mm. Similar to the explanation of the findings in the equal energy experiment, this can be explained by the fact that the acoustic energy applied in the experiments was the same. However, these findings might not be transferable to higher ablation volumes, when the focal spot in the indirect approach is placed further away from the surface of the phantom which could probably lead to irregularities in the heating pattern. Future experiments could focus on this topic.

Our research study has the following limitations: The bone phantom is in many ways intentionally kept simple unlike the natural conditions. For example, the surface of the polyurethane is simply flat where the bone of for example a vertebral body can form complex structures. Furthermore, the acoustic and thermal properties of polyurethane and especially the gel differ from bone and tissue. But for testing different transducers and treatment protocols, we searched for a most reliable and reproducible phantom being aware of deviating from real nature.

Another limitation of this study is the method of temperature readout: The temperature measurement method implemented in this study is based on the PRFS method and measurements are taken not directly on the surface of the phantom, but 4 mm parallel to the surface. This placement was chosen to ensure the best possible readout, since measurements directly on the surface are not feasible. The chemical composition of polyurethane does not allow temperature measurements in this material, which leads to incorrect measurements in all voxels which contain a relevant part of polyurethane (known as partial volume effect). This background explains the sometimes surprisingly low temperature elevation values, they would increase if measured directly at the surface. Measurements directly at the surface of the absorber are feasible with a thermocouple, but this method conflicts with the demand that the phantom should be easy to handle. Besides, our interest was to monitor reliability and therefore a consistency in temperature readout, which is covered by our chosen temperature measurement method.

The test of reproducibility was investigated in with a sonication duration of 20 s, which is the default sonication time on our MR-HIFU system. Conclusions for longer sonication times cannot be drawn from our study, since the linear model is does not cover an eventually occurring saturation and therefore asymptotic behaviour of temperature rise. But our model is applicable to the clinically important treatment duration, since for ablation treatments, which are currently the standard method of thermal therapy concerning bone related conditions, only short sonication durations are applied.

One limitation of the statistical methods is that the equal energy comparison and the treatment approach comparison were conducted with only a small number of repetitions (n=3) and

analysed with a descriptive statistic instead of an analytical one. Another limitation is that the equal energy comparison was only investigated for one energy value ($E_{acoustic}$ = 800 J) and might not be transferable to all energy settings. Nevertheless, these findings serve as a rough guideline and can be a base for future investigations.

We used a linear regression to characterize the heating curve in the reproducibility check in this thesis. A more accurate, but also more complex approach to model the temperature rise is the Pennes' bioheat equation.[126,127] But for the purpose of this thesis the linear regression turned out to be an adequate model for the investigated time- and temperature span.

Another apparent limitation, but also inspiration for future research is that the tests of the equal energy comparison and the treatment approach comparison were performed on a phantom. In vivo several other factors could influence the outcome of the experiment, e.g., as mentioned above the cooling effect of blood vessels.

The tests described in this thesis had only been conducted on a Sonalleve® system. Future studies could explore other system like Exablate® (Insightec Corp., Haifa, Israel) since the transducers differ in technical aspects. The comparison between indirect and direct approach has also been performed only on a Sonalleve® system, although the indirect approach is more used in Exablate® systems. Future experiments should focus on a comparison between different treatment sites, MR-HIFU systems and a more detailed investigation of the treatment approaches.

For training interventional radiologists for HIFU interventions or simulation of experimental treatments, we developed a phantom incorporating models of bone structures. Since the material polyurethane we used for the bone phantom is not 3D-printable, we investiagted other creative manufacturing schemes. One manufacturing scheme consists of segmentation, 3D printing of a mould and casting of liquid polyurethane. This manufacturing scheme is feasible and accurate but might seem effortful since the mould has to be destroyed in order to take the casted phantom out of the mould. This can be a problem especially for phantoms which one wants to produce in larger numbers. We met this argument by coming up with an alternative, more sustainable way of manufacturing based on silicone. A silicone mould was made as a negative from a 3D printed bone structure. The silicone form does not break when the casted phantom is removed and can thus be reused.

We performed a proof-of-concept study with two sonications on the swine facet joint phantom. The power levels were chosen according to successful swine facet joint ablations[91]. We found a higher peak temperature in the phantom experiments in comparison to the in vivo facet joint ablations, which can be explained by the lower absorption coefficient of the gel compared to muscle or fat tissue. The absorption coefficient of the polyurethane disk is also higher than the one of bone. Furthermore, the phantom does not have the cooling effect of blood perfusion.

The heating pattern along the surface of the facet joint model was comparable to a real swine treatment. Despite the deviations from in-vivo treatments, the facet joint model could serve as a model for planning complex treatments, in some cases as a substitution for animals in research or as a training model for interventional radiologists.
The developed phantom was designed for bone structures, but the process of segmentation is not limited to bone structures. The basic workflow of creating a phantom which consists of *segmentation – printing a mould – casting of a specific material* is theoretically extendable with several organ structures such as kidneys pancreas, brain structures etc.[128-130]

In conclusion, the developed bone phantom meets all our predefined criteria for a phantom: It is reusable, produces reliable measurements and is simple to handle. Thus, it can be used on the same MR-HIFU system before bone treatments to perform a quality assurance test. As a step further, it could be implemented to test different MR-HIFU systems on various treatment sites to ensure a similar heating pattern or to discover relevant differences between the systems. In this way, our bone phantom addresses the existing gap in quality assurance of MR-HIFU systems for bone applications.
The used material, polyurethane, is versatile and can be created in a more realistic way by a unique manufacturing method described in this study. The tests conducted for the facet joint phantom in this thesis were only a proof of concept, but it serves as a starting point for the development of an inexpensive and reusable tool for both training and research.

6. Literature

1. Breasted JH. The Edwin Smith Surgical Papyrus. *University of Chicago Oriental Institute Publications* 1930.
2. Wiemann B, Starnes CO. Coley's toxins, tumor necrosis factor and cancer research: a historical perspective. *Pharmacol Ther* 1994; **64**(3): 529-64.
3. Coley WB. The treatment of malignant tumors by repeated inoculations of erysipelas: with a report of ten original cases. *The American Journal of the Medical Sciences* 1893; **105**: 478-511.
4. Eggermont AM, de Wilt JH, ten Hagen TL. Current uses of isolated limb perfusion in the clinic and a model system for new strategies. *Lancet Oncol* 2003; **4**(7): 429-37.
5. Helderman R, Löke DR, Kok HP, et al. Variation in Clinical Application of Hyperthermic Intraperitoneal Chemotherapy: A Review. *Cancers (Basel)* 2019; **11**(1).
6. de Bree E, van Ruth S, Baas P, et al. Cytoreductive surgery and intraoperative hyperthermic intrathoracic chemotherapy in patients with malignant pleural mesothelioma or pleural metastases of thymoma. *Chest* 2002; **121**(2): 480-7.
7. Sousa A, Piñeiro I, Rodríguez S, et al. Recirculant hyperthermic IntraVEsical chemotherapy (HIVEC) in intermediate-high-risk non-muscle-invasive bladder cancer. *Int J Hyperthermia* 2016; **32**(4): 374-80.
8. Webb H, Lubner MG, Hinshaw JL. Thermal ablation. *Semin Roentgenol* 2011; **46**(2): 133-41.
9. Kok HP, Cressman ENK, Ceelen W, et al. Heating technology for malignant tumors: a review. *Int J Hyperthermia* 2020; **37**(1): 711-41.
10. Datta NR, Kok HP, Crezee H, Gaipl US, Bodis S. Integrating Loco-Regional Hyperthermia Into the Current Oncology Practice: SWOT and TOWS Analyses. *Front Oncol* 2020; **10**: 819.
11. Moyer HR, Delman KA. The role of hyperthermia in optimizing tumor response to regional therapy. *Int J Hyperthermia* 2008; **24**(3): 251-61.
12. Falk MH, Issels RD. Hyperthermia in oncology. *Int J Hyperthermia* 2001; **17**(1): 1-18.
13. Horsman MR, Overgaard J. Hyperthermia: a potent enhancer of radiotherapy. *Clin Oncol (R Coll Radiol)* 2007; **19**(6): 418-26.
14. Hurwitz MD. Hyperthermia and immunotherapy: clinical opportunities. *Int J Hyperthermia* 2019; **36**(sup1): 4-9.
15. Dewey WC. Arrhenius relationships from the molecule and cell to the clinic. *Int J Hyperthermia* 2009; **25**(1): 3-20.
16. Goldberg SN, Gazelle GS, Mueller PR. Thermal ablation therapy for focal malignancy: a unified approach to underlying principles, techniques, and diagnostic imaging guidance. *AJR Am J Roentgenol* 2000; **174**(2): 323-31.
17. Tempany CMC MN, Hynynen K, et al. Focused ultrasound surgery in oncology: Overview and principles. *Radiology* 2011; (259): 39–56.
18. Westra A, Dewey WC. Variation in sensitivity to heat shock during the cell-cycle of Chinese hamster cells in vitro. *Int J Radiat Biol Relat Stud Phys Chem Med* 1971; **19**(5): 467-77.
19. Law MP. Induced Thermal Resistance in the Mouse Ear: The Relationship between Heating Time and Temperature. *International Journal of Radiation Biology and Related Studies in Physics, Chemistry and Medicine* 1979; **35**(4): 481-5.
20. Sapareto SA, Dewey WC. Thermal dose determination in cancer therapy. *Int J Radiation Oncology* 1984; **10**: 787-800.
21. Bauer KD, Henle KJ. Arrhenius analysis of heat survival curves from normal and thermotolerant CHO cells. *Radiat Res* 1979; **78**(2): 251-63.
22. Overgaard J, Suit HD. Time-temperature relationship th hyperthermic treatment of malignant and normal tissue in vivo. *Cancer Res* 1979; **39**(8): 3248-53.
23. Yarmolenko PS, Moon EJ, Landon C, et al. Thresholds for thermal damage to normal tissues: an update. *Int J Hyperthermia* 2011; **27**(4): 320-43.
24. Roizin-Towle L, Pirro JP. The response of human and rodent cells to hyperthermia. *Int J Radiat Oncol Biol Phys* 1991; **20**(4): 751-6.

25. Dewhirst MW, Viglianti BL, Lora-Michiels M, Hanson M, Hoopes PJ. Basic principles of thermal dosimetry and thermal thresholds for tissue damage from hyperthermia. *Int J Hyperthermia* 2003; **19**(3): 267-94.
26. van Rhoon GC, Samaras T, Yarmolenko PS, Dewhirst MW, Neufeld E, Kuster N. CEM43 degrees C thermal dose thresholds: a potential guide for magnetic resonance radiofrequency exposure levels? *Eur Radiol* 2013; **23**(8): 2215-27.
27. Gawande A. Two hundred years of surgery. *N Engl J Med* 2012; **366**(18): 1716-23.
28. Kong CY, Meng L, Omer ZB, et al. MRI-guided focused ultrasound surgery for uterine fibroid treatment: a cost-effectiveness analysis. *AJR Am J Roentgenol* 2014; **203**(2): 361-71.
29. O'Sullivan AK, Thompson D, Chu P, Lee DW, Stewart EA, Weinstein MC. Cost-effectiveness of magnetic resonance guided focused ultrasound for the treatment of uterine fibroids. *Int J Technol Assess Health Care* 2009; **25**(1): 14-25.
30. Lynn JG, Zwemer RL, Chick AJ, Miller AE. A New Method for the Generation and Use of Focused Ultrasound in Experimental Biology. *J Gen Physiol* 1942; **26**(2): 179-93.
31. Haar GT, Coussios C. High intensity focused ultrasound: physical principles and devices. *Int J Hyperthermia* 2007; **23**(2): 89-104.
32. Siedek F, Yeo SY, Heijman E, et al. Magnetic Resonance-Guided High-Intensity Focused Ultrasound (MR-HIFU): Technical Background and Overview of Current Clinical Applications (Part 1). *Rofo* 2019; **191**(6): 522-30.
33. ter Haar G. Therapeutic applications of ultrasound. *Prog Biophys Mol Biol* 2007; **93**(1-3): 111-29.
34. Hynynen K, Jones RM. Image-guided ultrasound phased arrays are a disruptive technology for non-invasive therapy. *Phys Med Biol* 2016; **61**(17): R206-48.
35. ten Eikelder HM, Bosnacki D, Elevelt A, et al. Modelling the temperature evolution of bone under high intensity focused ultrasound. *Phys Med Biol* 2016; **61**(4): 1810-28.
36. Kim YS, Rhim H, Choi MJ, Lim HK, Choi D. High-intensity focused ultrasound therapy: an overview for radiologists. *Korean J Radiol* 2008; **9**(4): 291-302.
37. Sebeke LC, Rademann P, Maul AC, et al. Feasibility study of MR-guided pancreas ablation using high-intensity focused ultrasound in a healthy swine model. *Int J Hyperthermia* 2020; **37**(1): 786-98.
38. Wijlemans JW, Bartels LW, Deckers R, et al. Magnetic resonance-guided high-intensity focused ultrasound (MR-HIFU) ablation of liver tumours. *Cancer Imaging* 2012; **12**(2): 387-94.
39. Duck FA. The propagation of ultrasound through tissue. In: Haar Gt, ed. The Safe Use of Ultrasound in Medical Diagnoses. London: British Institute of Radiology; 2012.
40. Pennes HH. Analysis of tissue and arterial blood temperatures in the resting human forearm. 1948. *J Appl Physiol (1948)* 1948; **1**: 93-122.
41. Wissler EH. Pennes' 1948 paper revisited. *J Appl Physiol (1985)* 1998; **85**(1): 35-41.
42. Li S, Wu PH. Magnetic resonance image-guided versus ultrasound-guided high-intensity focused ultrasound in the treatment of breast cancer. *Chin J Cancer* 2013; **32**(8): 441-52.
43. Izadifar Z, Izadifar Z, Chapman D, Babyn P. An Introduction to High Intensity Focused Ultrasound: Systematic Review on Principles, Devices, and Clinical Applications. *J Clin Med* 2020; **9**(2).
44. Rieke V, Butts Pauly K. MR thermometry. *J Magn Reson Imaging* 2008; **27**(2): 376-90.
45. Ishihara Y, Calderon A, Watanabe H, et al. A Precise and Fast Temperature Mapping Using Water Proton Chemical Shift. *Magn Reson Med* 1995; **34**: 814-35.
46. De Poorter J, De Wagter C, De Deene Y, Thomsen C, Stahlberg F, Achten E. Noninvasive MRI thermometry with the proton resonance frequency (PRF) method: in vivo results in human muscle. *Magn Reson Med* 1995; **33**(1): 74-81.
47. Quesson B, de Zwart JA, Moonen CTW. Magnetic resonance temperature imaging for guidance of thermotherapy. *Journal of Magnetic Resonance Imaging* 2000; **12**(4): 525-33.
48. de Senneville BD, Mougenot C, Quesson B, Dragonu I, Grenier N, Moonen CT. MR thermometry for monitoring tumor ablation. *Eur Radiol* 2007; **17**(9): 2401-10.
49. Napoli A, Anzidei M, Ciolina F, et al. MR-guided high-intensity focused ultrasound: current status of an emerging technology. *Cardiovasc Intervent Radiol* 2013; **36**(5): 1190-203.
50. Coleman DJ, Lizzi FL, Silverman RH, et al. Therapeutic ultrasound. *Ultrasound in Medicine & Biology* 1986; **12**(8): 633-8.

51. Focused Ultrasound Foundation. State of the Field Report. 2022. http://www.fusfoundation.org/images/pdf/Focused_Ultrasound_Foundation_2022_State_of_the_Field_Report.pdf (accessed 12.03.2023).
52. Goss SA, Frizzell LA, Dunn F. Ultrasonic absorption and attenuation in mammalian tissues. *Ultrasound Med Biol* 1979; **5**(2): 181-6.
53. Nell DM, Myers MR. Thermal effects generated by high-intensity focused ultrasound beams at normal incidence to a bone surface. *J Acoust Soc Am* 2010; **127**(1): 549-59.
54. Pinton G, Aubry JF, Fink M, Tanter M. Effects of nonlinear ultrasound propagation on high intensity brain therapy. *Med Phys* 2011; **38**(3): 1207-16.
55. Kakhki VR, Anvari K, Sadeghi R, Mahmoudian AS, Torabian-Kakhki M. Pattern and distribution of bone metastases in common malignant tumors. *Nucl Med Rev Cent East Eur* 2013; **16**(2): 66-9.
56. Siegel RL, Miller KD, Jemal A. Cancer statistics, 2020. *CA Cancer J Clin* 2020; **70**(1): 7-30.
57. Huang JF, Shen J, Li X, et al. Incidence of patients with bone metastases at diagnosis of solid tumors in adults: a large population-based study. *Ann Transl Med* 2020; **8**(7): 482.
58. Galasko C. The anatomy and pathways of skeletal metastases. In: Weiss L GA, ed. Bone metastases. Boston: GK Hall; 1981: 49-63.
59. Coleman RE. Clinical features of metastatic bone disease and risk of skeletal morbidity. *Clin Cancer Res* 2006; **12**(20 Pt 2): 6243s-9s.
60. Rustoen T, Moum T, Padilla G, Paul S, Miaskowski C. Predictors of quality of life in oncology outpatients with pain from bone metastasis. *J Pain Symptom Manage* 2005; **30**(3): 234-42.
61. Portenoy RK. Pain and quality of life: clinical issues and implications for research. *Oncology (Williston Park)* 1990; **4**(5): 172-8; discussion 94.
62. Mantyh PW. Bone cancer pain: from mechanism to therapy. *Curr Opin Support Palliat Care* 2014; **8**(2): 83-90.
63. Leitlinienprogramm Onkologie (Deutsche Krebsgesellschaft DK, AWMF),. Interdisziplinäre Leitlinie der Qualität S3 zur Früherkennung, Diagnose und Therapie der verschiedenen Stadien des Prostatakarzinom. 2019. https://www.leitlinienprogramm-onkologie.de/leitlinien/prostatakarzinom (accessed 18.10.2020 2020).
64. Leitlinienprogramm Onkologie (Deutsche Krebsgesellschaft DK, AWMF),. Supportive Therapie bei onkologischen PatientInnen -Langversion 1.3. 2020. https://www.leitlinienprogramm-onkologie.de/leitlinien/supportive-therapie (accessed 18.10.2020 2020).
65. Huisman M, van den Bosch MA, Wijlemans JW, van Vulpen M, van der Linden YM, Verkooijen HM. Effectiveness of reirradiation for painful bone metastases: a systematic review and meta-analysis. *Int J Radiat Oncol Biol Phys* 2012; **84**(1): 8-14.
66. Cleeland CS, Gonin R, Hatfield AK, et al. Pain and its treatment in outpatients with metastatic cancer. *N Engl J Med* 1994; **330**(9): 592-6.
67. Chow E, Harris K, Fan G, Tsao M, Sze WM. Palliative radiotherapy trials for bone metastases: a systematic review. *J Clin Oncol* 2007; **25**(11): 1423-36.
68. Hartsell WF, Scott CB, Bruner DW, et al. Randomized trial of short- versus long-course radiotherapy for palliation of painful bone metastases. *J Natl Cancer Inst* 2005; **97**(11): 798-804.
69. Huisman M, Verkooijen HM, van der Linden YM, van den Bosch MA, van Vulpen M. Effectiveness of Repeat Radiotherapy for Painful Bone Metastases in Clinical Practice: A 10 Year Historical Cohort Study. *Clin Oncol (R Coll Radiol)* 2015; **27**(8): 472-8.
70. Gdowski AS, Ranjan A, Vishwanatha JK. Current concepts in bone metastasis, contemporary therapeutic strategies and ongoing clinical trials. *J Exp Clin Cancer Res* 2017; **36**(1): 108.
71. Yeo SY, Elevelt A, Donato K, et al. Bone metastasis treatment using magnetic resonance-guided high intensity focused ultrasound. *Bone* 2015; **81**: 513-23.
72. Gianfelice D, Gupta C, Kucharczyk W, Bret P, Havill D, Clemons M. Palliative treatment of painful bone metastases with MR imaging--guided focused ultrasound. *Radiology* 2008; **249**(1): 355-63.

73. Baal JD, Chen WC, Baal U, et al. Efficacy and safety of magnetic resonance-guided focused ultrasound for the treatment of painful bone metastases: a systematic review and meta-analysis. *Skeletal Radiol* 2021; **50**(12): 2459-69.
74. Yeo SY, Bratke G, Grüll H. High Intensity Focused Ultrasound for Treatment of Bone Malignancies—20 Years of History. *Cancers* 2022; **15**: 108.
75. Meeuse JJ, van der Linden YM, van Tienhoven G, et al. Efficacy of radiotherapy for painful bone metastases during the last 12 weeks of life: results from the Dutch Bone Metastasis Study. *Cancer* 2010; **116**(11): 2716-25.
76. Huisman M, ter Haar G, Napoli A, et al. International consensus on use of focused ultrasound for painful bone metastases: Current status and future directions. *Int J Hyperthermia* 2015; **31**(3): 251-9.
77. Harding D, Giles SL, Brown MRD, et al. Evaluation of Quality of Life Outcomes Following Palliative Treatment of Bone Metastases with Magnetic Resonance-guided High Intensity Focused Ultrasound: An International Multicentre Study. *Clin Oncol (R Coll Radiol)* 2018; **30**(4): 233-42.
78. Hurwitz MD, Ghanouni P, Kanaev SV, et al. Magnetic resonance-guided focused ultrasound for patients with painful bone metastases: phase III trial results. *J Natl Cancer Inst* 2014; **106**(5).
79. Hoy D, Bain C, Williams G, et al. A systematic review of the global prevalence of low back pain. *Arthritis Rheum* 2012; **64**(6): 2028-37.
80. Woolf AD PB. Burden of major musculoskeletal conditions. *Bull World Health Organ* 2003; **81**: 646-56.
81. Gellhorn AC, Katz JN, Suri P. Osteoarthritis of the spine: the facet joints. *Nat Rev Rheumatol* 2013; **9**(4): 216-24.
82. Schwarzer AC, Aprill CN, Derby R, Fortin J, Kine G, Bogduk N. Clinical features of patients with pain stemming from the lumbar zygapophysial joints. Is the lumbar facet syndrome a clinical entity? *Spine (Phila Pa 1976)* 1994; **19**(10): 1132-7.
83. Deutsche Gesellschaft für Orthopädie und Orthopädische Chirurgie (DGOOC). S2k Leitlinie Spezifischer Kreuzschmerz. 2018. https://www.awmf.org/uploads/tx_szleitlinien/033-051l_S2k_Spezifischer_Kreuzschmerz_2018-02.pdf (accessed 17.10.2020.
84. Manchikanti L, Abdi S, Atluri S, Benyamin RM, Hirsch JA. An Update of Comprehensive Evidence-Based Guidelines for Interventional Techniques in Chronic Spinal Pain. Part II: Guidance and Recommendations. *Pain Physician* 2013; **16**: 49-283.
85. Filippiadis DK, Kelekis A. A review of percutaneous techniques for low back pain and neuralgia: current trends in epidural infiltrations, intervertebral disk and facet joint therapies. *Br J Radiol* 2016; **89**(1057): 20150357.
86. Cohen SP, Huang JH, Brummett C. Facet joint pain--advances in patient selection and treatment. *Nat Rev Rheumatol* 2013; **9**(2): 101-16.
87. Datta S, Lee M, Falco FJ, Bryce DA, Hayek SM. Systematic assessment of diagnostic accuracy and therapeutic utility of lumbar facet joint interventions. *Pain Physician* 2009; **12**(2): 437-60.
88. Harnof S, Zibly Z, Shay L, et al. Magnetic resonance-guided focused ultrasound treatment of facet joint pain: summary of preclinical phase. *J Ther Ultrasound* 2014; **2**: 9.
89. Aginsky R, LeBlang S, Hananel A, et al. Tolerability and Feasibility of X-ray Guided Non-Invasive Ablation of the Medial Branch Nerve with Focused Ultrasound: Preliminary Proof of Concept in a Pre-clinical Model. *Ultrasound Med Biol* 2021; **47**(3): 640-50.
90. Browne JE, Tiegs-Heiden CA, Lehman VT, et al. Magnetic Resonance Imaging-Guided Focused Ultrasound Ablation of Lumbar Facet Joints of a Patient With a Magnetic Resonance Image Non-Conditional Pacemaker at 1.5T. *Mayo Clin Proc Innov Qual Outcomes* 2020; **4**(4): 464-8.
91. Tiegs-Heiden CA, Lehman VT, Gorny KR, Boon AJ, Hesley GK. Improved Treatment Response Following Magnetic Resonance Imaging-Guided Focused Ultrasound for Lumbar Facet Joint Pain. *Mayo Clin Proc Innov Qual Outcomes* 2020; **4**(1): 109-13.
92. Weeks EM, Platt MW, Gedroyc W. MRI-guided focused ultrasound (MRgFUS) to treat facet joint osteoarthritis low back pain--case series of an innovative new technique. *Eur Radiol* 2012; **22**(12): 2822-35.

93. Lee EH, Shafi M, Hui JHP. Osteoid Osteoma: A Current Review. *Journal of Pediatric Orthopaedics* 2006; **26**(5): 695-700.
94. Masciocchi C, Zugaro L, Arrigoni F, et al. Radiofrequency ablation versus magnetic resonance guided focused ultrasound surgery for minimally invasive treatment of osteoid osteoma: a propensity score matching study. *Eur Radiol* 2016; **26**(8): 2472-81.
95. Chen W, Zhu H, Zhang L, et al. Primary bone malignancy: effective treatment with high-intensity focused ultrasound ablation. *Radiology* 2010; **255**(3): 967-78.
96. Yarmolenko PS, Eranki A, Partanen A, et al. Technical aspects of osteoid osteoma ablation in children using MR-guided high intensity focussed ultrasound. *Int J Hyperthermia* 2018; **34**(1): 49-58.
97. Arrigoni F, Spiliopoulos S, de Cataldo C, et al. A Bicentric Propensity Score Matched Study Comparing Percutaneous Computed Tomography-Guided Radiofrequency Ablation to Magnetic Resonance-Guided Focused Ultrasound for the Treatment of Osteoid Osteoma. *J Vasc Interv Radiol* 2021; **32**(7): 1044-51.
98. Sharma KV, Yarmolenko PS, Celik H, et al. Comparison of Noninvasive High-Intensity Focused Ultrasound with Radiofrequency Ablation of Osteoid Osteoma. *J Pediatr* 2017; **190**: 222-8 e1.
99. Arrigoni F, Napoli A, Bazzocchi A, et al. Magnetic-resonance-guided focused ultrasound treatment of non-spinal osteoid osteoma in children: multicentre experience. *Pediatr Radiol* 2019; **49**(9): 1209-16.
100. Geiger D, Napoli A, Conchiglia A, et al. MR-guided focused ultrasound (MRgFUS) ablation for the treatment of nonspinal osteoid osteoma: a prospective multicenter evaluation. *J Bone Joint Surg Am* 2014; **96**(9): 743-51.
101. Parmeggiani A, Martella C, Ceccarelli L, Miceli M, Spinnato P, Facchini G. Osteoid osteoma: which is the best mininvasive treatment option? *Eur J Orthop Surg Traumatol* 2021; **31**(8): 1611-24.
102. Napoli A, Bazzocchi A, Scipione R, et al. Noninvasive Therapy for Osteoid Osteoma: A Prospective Developmental Study with MR Imaging-guided High-Intensity Focused Ultrasound. *Radiology* 2017; **285**(1): 186-96.
103. Kohler MO, Mougenot C, Quesson B, et al. Volumetric HIFU ablation under 3D guidance of rapid MRI thermometry. *Med Phys* 2009; **36**(8): 3521-35.
104. Zhou YF. High intensity focused ultrasound in clinical tumor ablation. *World J Clin Oncol* 2011; **2**(1): 8-27.
105. Bing F, Vappou J, de Mathelin M, Gangi A. Targetability of osteoid osteomas and bone metastases by MR-guided high intensity focused ultrasound (MRgHIFU). *Int J Hyperthermia* 2018; **35**(1): 471-9.
106. Odeen H, Parker DL. Magnetic resonance thermometry and its biological applications - Physical principles and practical considerations. *Prog Nucl Magn Reson Spectrosc* 2019; **110**: 34-61.
107. Ramsay E, Mougenot C, Kazem M, Laetsch TW, Chopra R. Temperature-dependent MR signals in cortical bone: potential for monitoring temperature changes during high-intensity focused ultrasound treatment in bone. *Magn Reson Med* 2015; **74**(4): 1095-102.
108. Lam MK, Huisman M, Nijenhuis RJ, et al. Quality of MR thermometry during palliative MR-guided high-intensity focused ultrasound (MR-HIFU) treatment of bone metastases. *J Ther Ultrasound* 2015; **3**: 5.
109. Shaw A, Martin E, Haller J, Ter Haar G. Equipment, measurement and dose-a survey for therapeutic ultrasound. *J Ther Ultrasound* 2016; **4**: 7.
110. Shaw A, Haar G. Requirements for measurement standards in high intensity focused ultrasound (HIFU) fields. 2006; 2006.
111. Zhou Y, Zhai L, Simmons R, Zhong P. Measurement of high intensity focused ultrasound fields by a fiber optic probe hydrophone. *J Acoust Soc Am* 2006; **120**(2): 676-85.
112. Hill CR, Rivens I, Vaughan MG, Ter Haar GR. Lesion development in focused ultrasound surgery: A general model. *Ultrasound in Medicine & Biology* 1994; **20**(3): 259-69.
113. ter Haar G, Shaw A, Pye S, et al. Guidance on reporting ultrasound exposure conditions for bio-effects studies. *Ultrasound Med Biol* 2011; **37**(2): 177-83.

114. Bini MG, Ignesti A, Millanta L, Olmi R, Rubino N, Vanni R. The polyacrylamide as a phantom material for electromagnetic hyperthermia studies. *IEEE Trans Biomed Eng* 1984; **31**(3): 317-22.
115. Lafon C, Zderic V, Noble ML, et al. Gel phantom for use in high-intensity focused ultrasound dosimetry. *Ultrasound Med Biol* 2005; **31**(10): 1383-9.
116. Eranki A, Mikhail AS, Negussie AH, Katti PS, Wood BJ, Partanen A. Tissue-mimicking thermochromic phantom for characterization of HIFU devices and applications. *Int J Hyperthermia* 2019; **36**(1): 518-29.
117. Negussie AH, Partanen A, Mikhail AS, et al. Thermochromic tissue-mimicking phantom for optimisation of thermal tumour ablation. *Int J Hyperthermia* 2016; **32**(3): 239-43.
118. Okada A, Morita Y, Fukunishi H, Takeichi K, Murakami T. Non-invasive magnetic resonance-guided focused ultrasound treatment of uterine fibroids in a large Japanese population: impact of the learning curve on patient outcome. *Ultrasound Obstet Gynecol* 2009; **34**(5): 579-83.
119. Huisman M, Lam MK, Bartels LW, et al. Feasibility of volumetric MRI-guided high intensity focused ultrasound (MR-HIFU) for painful bone metastases. *J Ther Ultrasound* 2014; **2**: 16.
120. ter Haar G. Safety first: progress in calibrating high-intensity focused ultrasound treatments. *Imaging in Medicine* 2013; **5**(6): 567-75.
121. Fedorov A, Beichel R, Kalpathy-Cramer J, et al. 3D Slicer as an image computing platform for the Quantitative Imaging Network. *Magnetic Resonance Imaging* 2012; **30**(9): 1323-41.
122. Rossum GV. Python tutorial. *Centrum voor Wiskunde en Informatica (CWI)* 1995.
123. Newville M, Stensitzki, Till, Allen, Daniel B., & Ingargiola, Antonino. LMFIT: Non-Linear Least-Square Minimization and Curve-Fitting for Python (Version 0.8.0). *Zenodo* 2014.
124. Meshorer A, Prionas SD, Fajardo LF, Meyer JL, Hahn GM, Martinez AA. The effects of hyperthermia on normal mesenchymal tissues. Application of a histologic grading system. *Arch Pathol Lab Med* 1983; **107**(6): 328-34.
125. Schneider CA, Rasband WS, Eliceiri KW. NIH Image to ImageJ: 25 years of image analysis. *Nature Methods* 2012; **9**(7): 671-5.
126. Wu J, Chase JD, Zhu Z, Holzapfel TP. Temperature rise in a tissue-mimicking material generated by unfocused and focused ultrasonic transducers. *Ultrasound Med Biol* 1992; **18**(5): 495-512.
127. Chen D, Fan T, Zhang D, Wu J. A feasibility study of temperature rise measurement in a tissue phantom as an alternative way for characterization of the therapeutic high intensity focused ultrasonic field. *Ultrasonics* 2009; **49**(8): 733-42.
128. Kumar H, DeSouza SV, Petrov MS. Automated pancreas segmentation from computed tomography and magnetic resonance images: A systematic review. *Comput Methods Programs Biomed* 2019; **178**: 319-28.
129. González-Villà S, Oliver A, Valverde S, Wang L, Zwiggelaar R, Lladó X. A review on brain structures segmentation in magnetic resonance imaging. *Artificial Intelligence in Medicine* 2016; **73**: 45-69.
130. Torres HR, Queirós S, Morais P, Oliveira B, Fonseca JC, Vilaça JL. Kidney segmentation in ultrasound, magnetic resonance and computed tomography images: A systematic review. *Comput Methods Programs Biomed* 2018; **157**: 49-67.
131. Virtanen P, Gommers R, Oliphant TE, et al. SciPy 1.0: fundamental algorithms for scientific computing in Python. *Nat Methods* 2020; **17**(3): 261-72.
132. Chatterjee S. Residuals. In: Lovric M, ed. International Encyclopedia of Statistical Science. Berlin, Heidelberg: Springer Berlin Heidelberg; 2011: 1227-9.

7. Appendix

7.1 List of figures

7.2 List of tables

7.3 Acoustic properties of the polyurethane disk and polyacrylamide gel

Table 6 shows the acoustic properties of the components of the bone phantom (polyurethane disk and polyacrylamide gel) in comparison to their natural counterparts (cortical bone and tissue like muscle/fat).

Table 6: Thermal and acoustic parameters for polyurethane, gel, cortical bone and tissues like muscle or fat. Data for bone and tissue were derived from Hasgall et al. and Shankar et al.132,133 The minimum and maximum value found in literature/ the experiments

	Polyurethane Disk	**Cortical bone**	**Polyacryl-amide gel**	**Muscle/ fat**
Thermal conductivity [W/mK]	0.30-0.31	0.3-0.36	0.60-0.64	0.42-0.56/ 0.18-0.24
Speed of sound [m/s]	1356-1557	2660-4200	1516-1567	1545-1631/ 1412-1490
Attenuation coefficient [dB/cm/MHz]	34.9-115.0	4.74	0.019-0.044	0.38

7.4 Statistical analysis

7.4.1. Reproducibility

The temperature evolution in the reproducibility experiments was investigated by performing a linear regression of the mean and maximum temperature values in the ROI over the sonication time (stats.linregress module, scipy python package version 1.1.0).[131]

The quality of the regression over all measurement points was described by the standard error (SE) of the estimated slope and the correlation coefficient R^2. While R^2 represents the proportion of the variance which can be explained by the linear model, the standard error is a measure of the variance of the slope.

To describe the variance of the individual measurement points, the residuals were graphically displayed. Residuals (R) were calculated by the following equation[132]:

$$R = y - \hat{y}$$

With y as the individual measurement point and $\hat{y}$ as the respective point at the linear regression curve over all measurement points.

The reliability over time was investigated by performing a linear regression (package see above) over the temperature measurements at the end of each sonication (19.4 s). The slope and the correlation coefficient were taken as an indicator for reproducibility of the experiments.

7.4.2. Power dependence

A linear regression was performed using the stats.linregress module of the scipy python package version 1.1.0.[131] The correlation between applied power and temperature difference at the end of the sonication was quantified by a linear fit of the slope values of a linear fit of the heating curve in each power setting.

7.4.3. Equal energy comparison

Comparison between equal energy doses but different time/ power settings (treatment with 40W power and 20s treatment time opposed to 20W power and 40s treatment time) was done by first calculating the mean value and the standard deviation of the volume of a CEM43 value ≥ 240 min of the approximated spheroid. The difference of the mean values of the two approaches was then calculated. A two-sided independent-samples t-test (stats.ttest_indl module, scipy python package version 1.1.0)[131] was done in order to investigate if there is a significant difference between the two different power and sonication time settings.

7.4.4. Indirect/ direct approach comparison

Comparison between indirect and direct approach was done similar to the equal energy comparison: First, the mean value and the standard deviation of the volume of a CEM43 value ≥ 240 min of the approximated spheroid was calculated. After that, the difference of the mean values of the two approaches was calculated. A two-sided independent-samples t-test (stats.ttest_rel module, scipy python package version 1.1.0)[131] was done in order to investigate if there is a significant difference between the different treatment approaches.

8. List of publications

Conference abstract:

Strobel J, Sebeke L, Heijman E, Grüll H: Standardised method to calibrate multivendor MR-HIFU systems used in randomised controlled trial of bone pain palliation study. 7th International Symposium on Focused Ultrasound, online edition, 2020